RESOURCE
https://doi.org/10.1038/s41591-018-0207-3

nature medicine

A biobank of patient-derived pediatric brain tumor models

Sebastian Brabetz[1,2,3,16], Sarah E. S. Leary[4,5,16], Susanne N. Gröbner[1,2,16], Madison W. Nakamoto[5], Huriye Şeker-Cin[2], Emily J. Girard[5], Bonnie Cole[4], Andrew D. Strand[5], Karina L. Bloom[5], Volker Hovestadt[6,7,8], Norman L. Mack[1,2,6], Fiona Pakiam[5], Benjamin Schwalm[1,2], Andrey Korshunov[9,10], Gnana Prakash Balasubramanian[1,2], Paul A. Northcott[2,11], Kyle D. Pedro[5], Joyoti Dey[5,14], Stacey Hansen[5], Sally Ditzler[5], Peter Lichter[6], Lukas Chavez[1,2,15], David T. W. Jones[1,2], Jan Koster[12], Stefan M. Pfister[1,2,13,17*], Marcel Kool[1,2,17*] and James M. Olson[4,5,17*]

Brain tumors are the leading cause of cancer-related death in children. Genomic studies have provided insights into molecular subgroups and oncogenic drivers of pediatric brain tumors that may lead to novel therapeutic strategies. To evaluate new treatments, better preclinical models adequately reflecting the biological heterogeneity are needed. Through the Children's Oncology Group ACNS02B3 study, we have generated and comprehensively characterized 30 patient-derived orthotopic xenograft models and seven cell lines representing 14 molecular subgroups of pediatric brain tumors. Patient-derived orthotopic xenograft models were found to be representative of the human tumors they were derived from in terms of histology, immunohistochemistry, gene expression, DNA methylation, copy number, and mutational profiles. In vivo drug sensitivity of targeted therapeutics was associated with distinct molecular tumor subgroups and specific genetic alterations. These models and their molecular characterization provide an unprecedented resource for the cancer community to study key oncogenic drivers and to evaluate novel treatment strategies.

Brain tumors are the most common solid tumors in children and the leading cause of pediatric cancer death. Three broad histologic tumor categories comprise the majority of malignant pediatric brain tumors: embryonal tumors such as medulloblastoma (MB) and atypical teratoid/rhabdoid tumors (ATRT), high-grade glioma (HGG), and ependymoma (EPN). Genomic and epigenomic studies have greatly expanded our understanding of the underlying biology and genetics of these tumors, and have identified clinically relevant molecular subgroups, some of which should rather be considered completely distinct diseases[1–8]. Emphasizing the importance of integrating molecular and histological diagnoses, molecular classification has already been translated into standard clinical practice for MB[9]. For other tumors, such as EPN, molecular subgrouping is strongly recommended for future clinical trials[10,11].

Molecular subgroups of the various histological entities are characterized by different driver mutations and differences in demographics, outcome, and response to targeted therapies[12], and they are probably derived from different cellular origins[13]. Taken together this strongly suggests that they may also need to be treated differently. It is therefore essential to acknowledge and study pediatric brain tumors as a group of distinct rare diseases, particularly in the context of novel targeted therapeutic development. To develop such new strategies in preclinical studies, well-characterized model systems representing the entire biological spectrum are needed.

Thorough preclinical studies of cancer therapeutics in appropriate models are essential in order to identify and prioritize candidates for further evaluation in humans. Preclinical models are of particular importance in rare disease, including all pediatric brain tumors, where human trials may take more than a decade to complete in order to compare two treatment arms[14]. In adult oncology, large cohorts of patient-derived xenograft (PDX) models have already been established to function as a preclinical platform and tool to study tumor biology[15–17]. Importantly, the '$n=1$' approach with these models allows high-throughput in vivo evaluation of drug responses and has been shown to be predictive of clinical trials[15]. Preclinical trials using well-characterized PDX models will therefore be essential to identify therapeutic candidates of interest and potential target patient populations. Perhaps most importantly, the use of well-characterized mouse models may deprioritize the use of agents in patient groups where they are unlikely to be

[1]Hopp Children's Cancer Center, NCT Heidelberg (KiTZ), Heidelberg, Germany. [2]Division of Pediatric Neurooncology, German Cancer Consortium (DKTK), German Cancer Research Center (DKFZ), Heidelberg, Germany. [3]Faculty of Biosciences, Heidelberg University, Heidelberg, Germany. [4]Seattle Children's and University of Washington, Seattle, WA, USA. [5]Clinical Research Division, Fred Hutchinson Cancer Research Center, Seattle, WA, USA. [6]Division of Molecular Genetics, German Cancer Consortium (DKTK), German Cancer Research Center (DKFZ), Heidelberg, Germany. [7]Department of Pathology and Center for Cancer Research, Massachusetts General Hospital and Harvard Medical School, Boston, MA, USA. [8]Broad Institute of MIT and Harvard, Cambridge, MA, USA. [9]CCU Neuropathology, German Cancer Research Center (DKFZ), Heidelberg, Germany. [10]Department of Neuropathology, Heidelberg University, Heidelberg, Germany. [11]Department of Developmental Neurobiology, St Jude Children's Research Hospital, Memphis, TN, USA. [12]Department of Oncogenomics, Academic Medical Center, Amsterdam, The Netherlands. [13]Department of Pediatric Oncology, Hematology and Immunology, Heidelberg University Hospital, Heidelberg, Germany. [14]Present address: Presage Biosciences, Seattle, WA, USA. [15]Present address: Department of Medicine, Division of Medical Genetics, University of California San Diego School of Medicine, La Jolla, CA, USA. [16]These authors contributed equally: Sebastian Brabetz, Sarah E. S. Leary, Susanne N. Gröbner. [17]These authors jointly supervised this work: Stefan M. Pfister, Marcel Kool, James M. Olson. *e-mail: s.pfister@kitz-heidelberg.de; m.kool@kitz-heidelberg.de; jolson@fredhutch.org

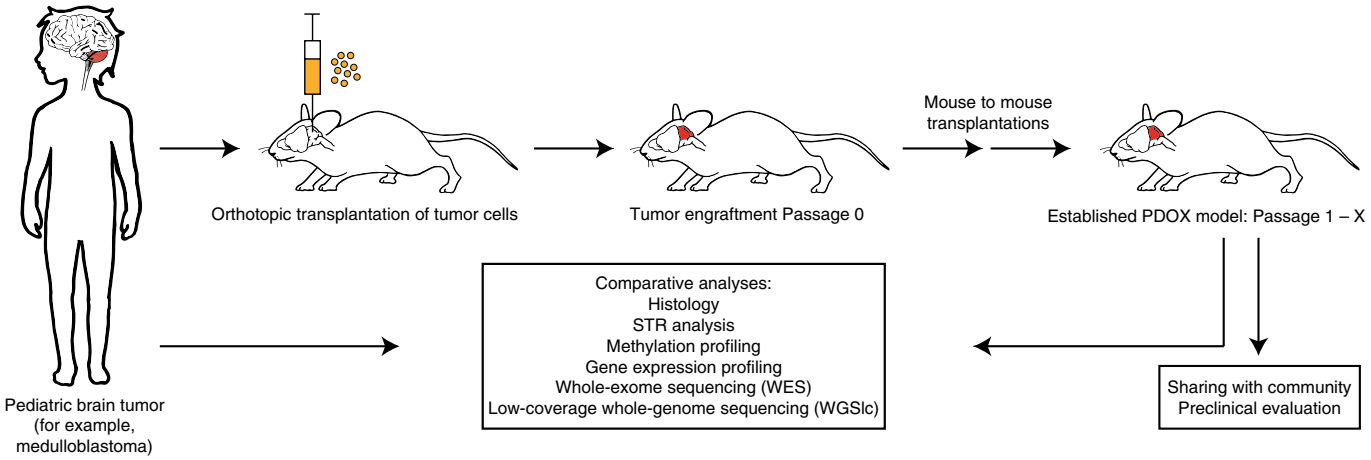

Fig. 1 | PDOX of pediatric brain tumors. Schematic illustration of the establishment and characterization pipeline of PDOX models of pediatric brain tumors with an example of a tumor located in the posterior fossa (for example, MB). Tumors were injected in the brain region of the mice corresponding to the location of the tumors in the patients.

effective, thus avoiding wasted patient lives, time, and money on predictably ineffective therapies. However, similar approaches in pediatric oncology are lagging behind owing to the rarity of the disease. The few PDX models of pediatric brain cancer described so far do not adequately represent the multitude of brain tumor subgroups. Moreover, existing models have often been established as in vitro cultures, have not (or only to some extent) been characterized at a molecular level, and often do not grow orthotopically[18–20].

Here, we describe 30 molecularly characterized patient-derived orthotopic xenograft (PDOX) models and seven cell lines of multiple pediatric brain tumor subgroups developed through the Children's Oncology Group ACNS02B3 brain tumor biology study. As a rare and valuable resource, we offer to share these models with the scientific community to facilitate further investigation of tumor biology and evaluation of potential cancer therapeutics.

Results

Tumor engraftment. PDOX lines were created from freshly obtained pediatric brain tumor specimens collected between 2009 and 2014 (Fig. 1). In total, 100 patient tumor samples were orthotopically implanted into NOD-scid IL2Rgamma^{null} (NSG) mice, of which 30 (30%) engrafted and were amenable to serial passaging. The engraftment rate was 37% (15/41) for MB, 25% (2/8) for ATRT, 29% (2/7) for other embryonal tumors, 17% (3/18) for EPN, and 31% (8/26) for HGG (Supplementary Fig. 1a). In our cohort, engraftment rates did not vary significantly between patient samples being implanted within hours after surgery (28%; 14/50) and patient samples being shipped overnight (32%; 16/50) (Supplementary Fig. 1b). In six additional instances (6%; 6/100), we observed development of mouse tumors of hematopoietic origin within the brain as described in other entities and mouse strains[21,22]. These tumors had an extremely short latency of less than 3 weeks, were clearly identified as nonhuman by histologic appearance as well as immunohistochemical staining, and failed in short tandem repeat (STR) analysis. STR analysis was also used for quality control to confirm genotype matching between human tumor and PDOX passages. Of the 30 models described here, the majority of tumors (22) were obtained from surgery at the time of primary diagnosis; three from surgery of recurrent tumors and five from patient autopsies (Supplementary Table 1). The interval from implantation of human tumor to presentation of cranial bulge or tumor-related symptoms in mice was highly variable. In the initial human-to-mouse passage, referred to as P0, tumors were observed in as little as 41 days and as long as 326 days. As tumors were serially passaged in mice, there was a trend toward shorter latency (Supplementary Table 1). At later passages, tumor latency was nearly identical between animals in each line, but varied between different histology-based tumor entities, as well as between molecular subgroups of disease of similar histology. To confirm that our PDOX repertoire can be readily shared with the research community, we tested whether PDOX lines regrow after cryopreservation and storage in liquid nitrogen. All 22 PDOX lines tested could be revived, while 98% (52/53) of thawing events were successful with variable engraftment rates per thawing event (Supplementary Fig. 1c). Finally, we also generated seven stable cell lines, four from tumors that also engrafted as PDOX and three from tumors that did not engraft as a PDOX (independent cell lines). All cell lines were established directly from the human tumor and passaged at least ten times.

Tumor histology. Histologically, PDOX tumors closely resemble the human tumors from which they are derived. Representative comparative histology and immunohistochemical stains from several primary human tumors and PDOX models are shown in Fig. 2.

For instance, the characteristic pseudorosette formation present in primary EPN was maintained in the corresponding PDOX model. Positive synaptophysin staining, typically seen in MB tumors, was still present in the MB PDOX models. Also, molecular alterations detected by immunohistochemistry were maintained in the corresponding PDOX models, such as the absence of SMARCB1/INI1 expression in the ATRT models or, in HGG or PNET models, the nuclear accumulation of TP53 or overexpression of EGFR. More detailed histological information for the PDOX models is available in Supplementary Table 2 and the online PDX Explorer (http://www.r2platform.com/pdxexplorer) as described below.

Molecular classification and characterization of PDOX models and cell lines. DNA methylation profiles were used to classify all models ($n=30$ early passage [P1-2], $n=23$ late passage [P4-5], $n=7$ cell lines) and matching human tumors ($n=22$) to tumor type and molecular subgroup[2,8,11,23,24] (Supplementary Table 3). *t*-Distributed stochastic neighbor embedding (*t*-SNE) analysis of our methylation profiles, supplemented with 226 reference profiles representing various distinct molecular subgroups of pediatric brain tumors, robustly grouped the preclinical models into the subgroups of MB, HGG, ATRT, EPN, and pineoblastoma (PB) (Fig. 3). Methylation profiling identified 15 MB PDOX models, comprising one MB-WNT, four

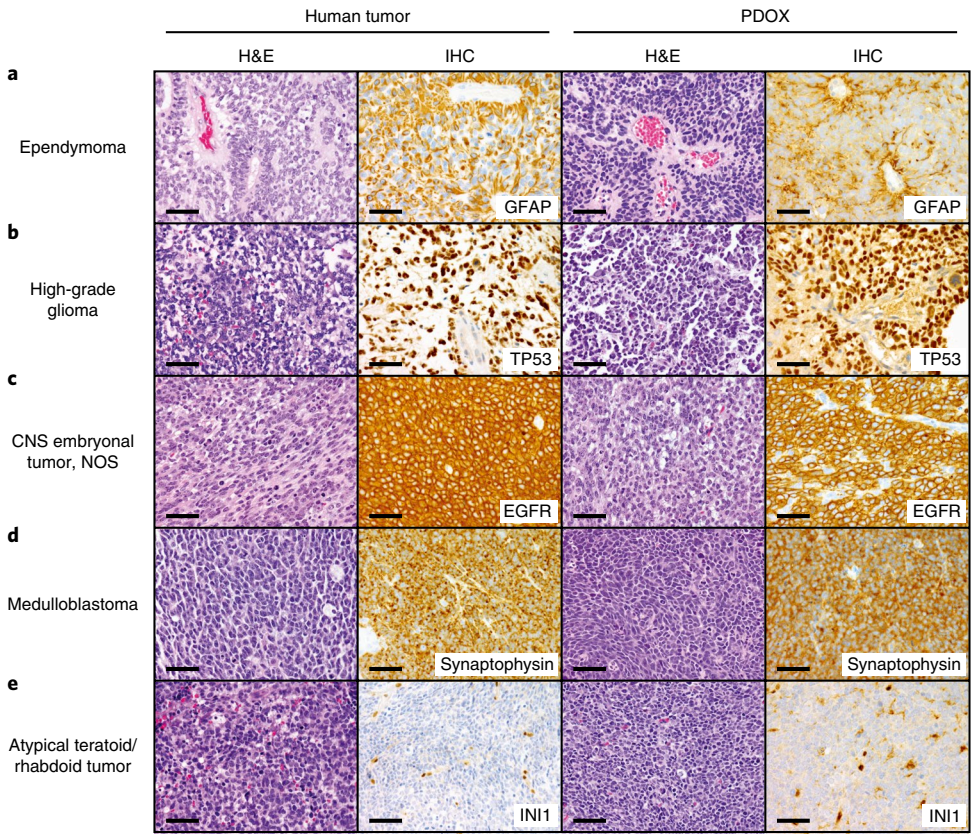

Fig. 2 | Histology and immunohistochemistry are conserved in PDOX. Representative comparative histology showing stable morphologic appearance of PDOX tumors in reference to the human tumor used to generate the PDOX. Scale bar, 50 µm. $n = 16$ biologically independent PDOX lines have been compared with their matching human tumors as listed in Supplementary Table 2.

MB-SHH, seven MB-Group3, and three MB-Group4; eight HGG models, two of the K27 subgroup, two of the recently described MYCN subgroup, and four models of the pedRTK1 subgroup[25]; three EPN PDOX models, two of the PFA subgroup, and one of the RELA subgroup; two ATRT PDOX, one of the SHH subgroup and one of the MYC subgroup; and two PB PDOX models (Fig. 3). The three independent cell lines classified as one HGG-pedRTK1, one HGG-pedRTK2, and one ATRT-SHH line (Fig. 3). Except for three cases, the molecular classification was in line with the histological diagnosis. One PNET (PBT-06FH) was reclassified as a HGG-pedRTK1 model; two tumors with embryonal pathology, diagnosed as MB (PBT-04FH) and supratentorial PNET (PBT-05FH), were both molecularly classified as HGG-MYCN tumors. Both these tumors and the associated PDOX lines harbored *MYCN* and *ID2* amplifications, characteristic for this molecular subgroup of HGGs[24,25] (Supplementary Fig. 2a,b). To elucidate whether later PDOX passages and cell lines from the same tumors equally recapitulate the tumor subgroups, we added methylation profiles of later PDOX passages ($n = 23$) and matched cell lines ($n = 4$) to the analysis (Supplementary Table 3). Patient tumor, corresponding early and late PDOX tumors, and matching cell lines mapped closely together within their respective cluster (Supplementary Fig. 3), confirming that both later PDOX passages and the primary cell cultures faithfully recapitulated the original disease. In summary, we have established and fully characterized 30 PDOX models in addition to four matched cell lines and three independent cell lines, representing 14 distinct molecular subgroups of pediatric brain tumors.

Genomic landscape of PDOX models and cell lines. To select the most appropriate PDOX model or cell line for some preclinical studies, it is essential to know the underlying mutation pattern of disease-relevant oncogenes and tumor suppressor genes, even after accounting for molecular subgroups. Therefore, we performed whole-exome sequencing and low-coverage whole-genome sequencing for all 30 PDOX models, the three independent cell lines, and, whenever available, for the matching human tumors ($n = 19$) (Supplementary Table 3). In addition, we validated potential driver events in later PDOX passages via Sanger sequencing and by generating copy-number profiles from DNA methylation array data (Fig. 4 and Supplementary Table 4). As matching germline controls were unavailable for our series of PDOX models, we were unable to comprehensively call somatic variants in this study. Hence, we filtered for variants with a minor allele frequency of less than 0.1% in the population and highlighted cancer genes recurrently mutated in the specific tumor entities, as identified in previous sequencing studies[26,27]. To avoid false positive mutation calls, we aligned all sequencing reads to a combined human and mouse reference genome and neglected all reads aligned to the mouse genome[17,28]. The results from this method were benchmarked against alignment to the human reference genome only. Indeed, mutation calling in our cohort of 19 human tumor and PDOX pairs resulted in far more mutation calls (6,577) after aligning only to the human genome than after alignment to a merged reference (2,537) (Supplementary Fig. 4a). Of the human alignment-exclusive mutations 92.43% (3,734/4,040) were found only in the PDOX and not in the matching human tumor (Supplementary Fig. 4a). To prove that these additional mutations are artifacts induced by mouse reads, we performed whole-exome sequencing on mouse tissue, aligned the reads to only the human genome, and performed variant calling. These artifacts overlapped with 98% of the mutations exclusive to

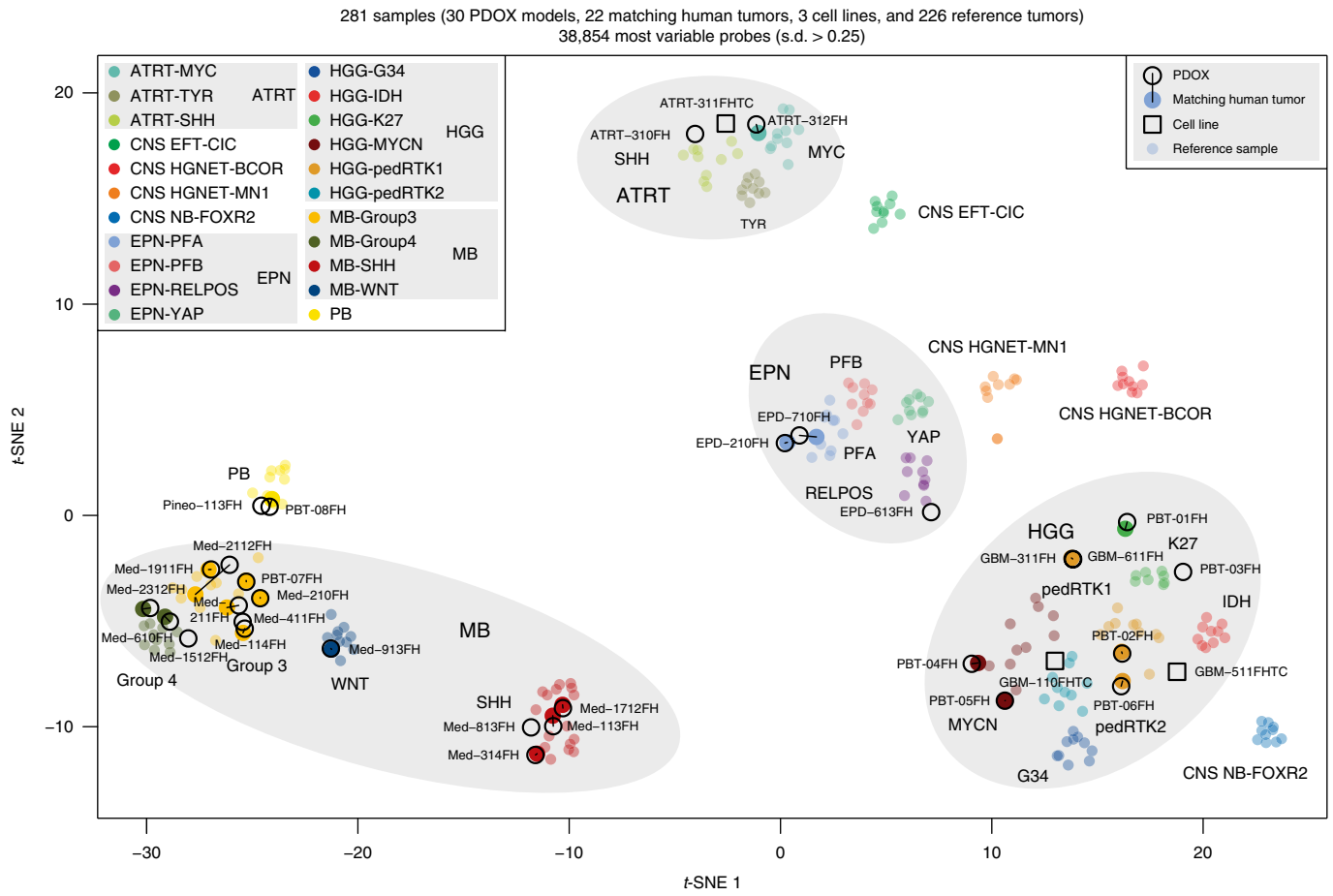

Fig. 3 | Molecular subgrouping of PDOX models and cell lines. 2D representation of pairwise sample correlations using the 38,854 most variably methylated probes (s.d. > 0.25) by *t*-SNE dimensionality reduction. The total number of samples was 281, consisting of 30 early PDOX passages, 22 matching human tumors, 3 patient-derived cell lines, and 226 reference cases. Reference samples are colored according to their molecular reference entity. Early PDOX passages are shown as black circles, cell lines as black rectangles. Matching human tumors are colored according to their molecular entity and are linked to the matching preclinical model with black lines. Positions of individual samples within the plot are available in Supplementary Table 3.

the human alignment and did not overlap with mutations shared between both alignment methods or with mutations exclusive to alignment to the merged genome (Supplementary Fig. 4b).

The sequencing analyses showed that all models harbored genetic alterations characteristic for the respective disease (Fig. 4). Important driver genes, present in the human tumors, were typically retained in the different passages of the PDOX models and in the cell lines. For instance, the MB-WNT model Med-913FH contains the prototypical *CTNNB1* mutation and two MB-SHH lines are driven by mutation/loss of *PTCH1*, while the two other MB-SHH lines show characteristic *MYCN* and *GLI2* amplifications in combination with a *TP53* mutation (Fig. 4a). Five of our MB-Group3 lines harbor *MYC* amplifications, while two lines have high *MYC* expression without an accompanying *MYC* amplification. One of these two lines, PBT-07FH, carries the hotspot insertion in *KBTBD4*[27]. The *MYC*-amplified line Med-211FH additionally shows *GFI1B* activation, caused by enhancer hijacking as previously described[29] (Supplementary Fig. 5a,b). Another enhancer hijacking event was identified for *PRDM6* in the MB-Group4 model Med-610FH, as described recently[27] (Supplementary Fig. 5c,d). The two HGG-K27 models, PBT-01FH and PBT-03FH, both harbor K27M mutations in *H3F3A* and *HIST1H3B*, respectively. Both HGG-MYCN models carry *MYCN* and *ID2* coamplifications, but only PBT-05FH presents with an additional *EGFR* amplification (Fig. 4b). Two HGG-pedRTK1 models, GBM-311FH and GBM-611FH, generated from primary and autopsy tumor, respectively, from the same patient, both harbor *MSH2* mutations, resulting in a hypermutator phenotype (Supplementary Fig. 5e). The two other HGG-pedRTK1 models, PBT-02 and PBT-06FH, both carry *CDK4* amplifications, but only one (PBT-06FH) additionally harbors the typical *PDGFRA* amplification and a *TP53* mutation (Fig. 4b). The EPN-PFA models express *CXorf67*, but did not harbor the recently described mutations[30]. In addition, both models show gain of chromosome 1q, which is associated with a poor prognosis in this disease[31] (Fig. 4c). In the EPN-RELA model, EPD-613FH, the presence of the defining *C11orf95-RELA* fusion (type 1) was confirmed by RNA-seq[32] (Supplementary Fig. 5f). In addition, loss of *CDKN2A/B* was observed, which is also often seen in this molecular subgroup[11] (Fig. 4c). Finally, both ATRT models showed characteristic *SMARCB1* inactivation[33] (Fig. 4d). Systematic evaluation of all predicted somatic single-nucleotide variants showed that, on average, 97.73 ± 0.99% of all mutations were maintained from the patient tumor to the PDOX (Supplementary Fig. 5g), and, on average, 4.44% ± 2.22% of all mutations in the PDOX were not found in the patient tumor (Supplementary Fig. 5h).

Regarding the three independent cell lines (for which PDOX tumors did not engraft), we found that both HGG cell lines have a *CDKN2A/B* loss, while only the pedRTK2 cell line, GBM-110FHTC, additionally harbors a *BRAF* V600E mutation, which is actually uncommon for pedRTK2 tumors[25]. The ATRT cell line, ATRT-311FHTC, shows a typical loss of *SMARCB1*.

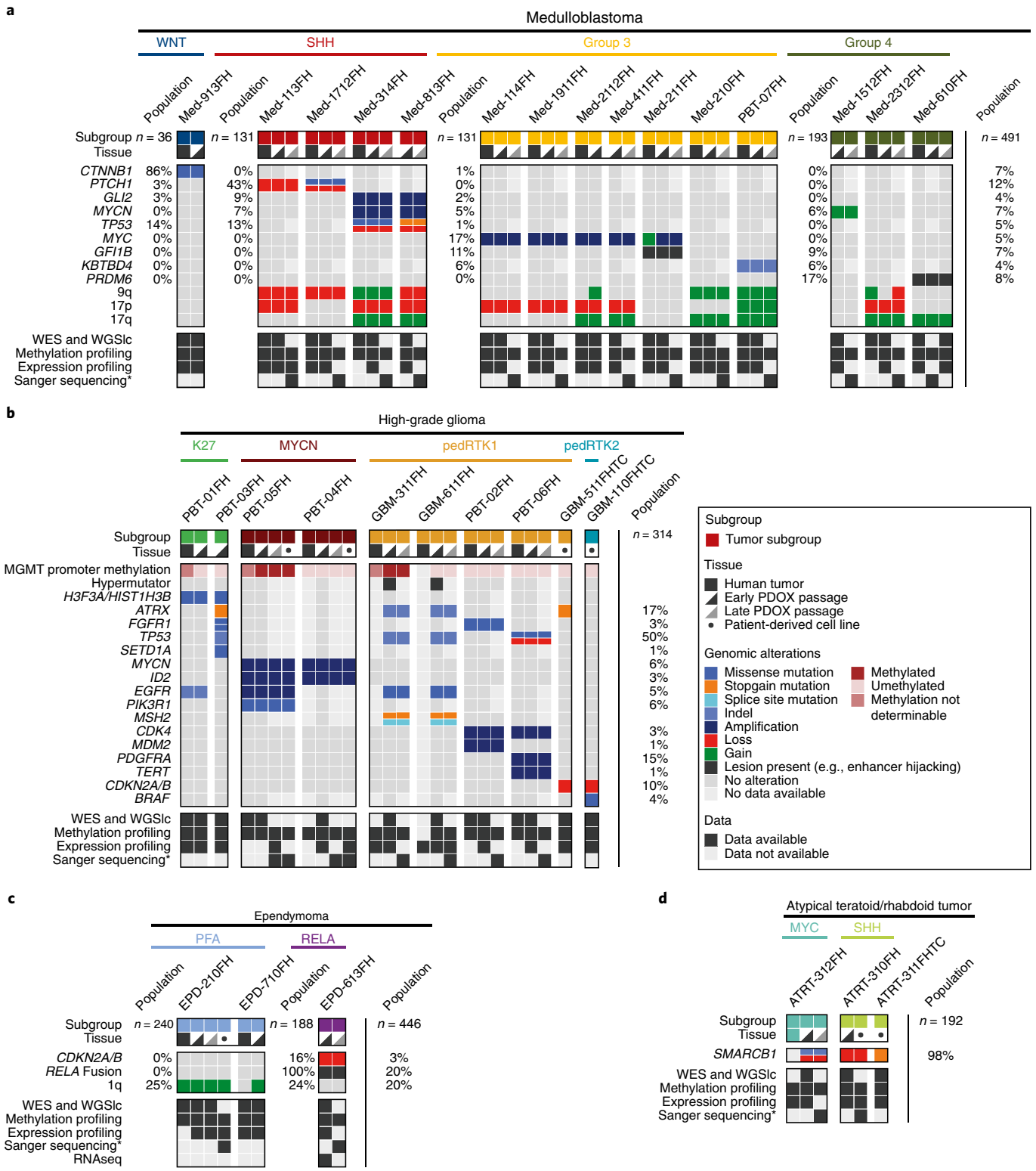

Fig. 4 | Molecular characterization of PDOX models and cell lines. a–d,Hallmark genomic alterations, including chromosomal changes, amplifications, deletions, and mutations, are persistent between human tumor, PDOX models at early and late passages, and patient-derived cell lines in MB (**a**), HGG (**b**), EPN (**c**), and ATRT (**d**). Population frequencies are based on human tumor cohorts (MB: Northcott et al.[27]; HGG: Mackay et al.[26]; EPN: Pajtler et al.[11]; ATRT: Johann et al.[2]). *Potential driver mutations with an allele frequency of at least 0.2 in early PDOX passages were validated in late PDOX passages by Sanger sequencing.

A full list of all identified events in PDOX models, cell lines, and matching human tumors is presented in Supplementary Table 4. Altogether, these analyses show that our repertoire not only represents various distinct molecular subgroups of pediatric brain tumors, but also intertumor molecular heterogeneity within these subgroups.

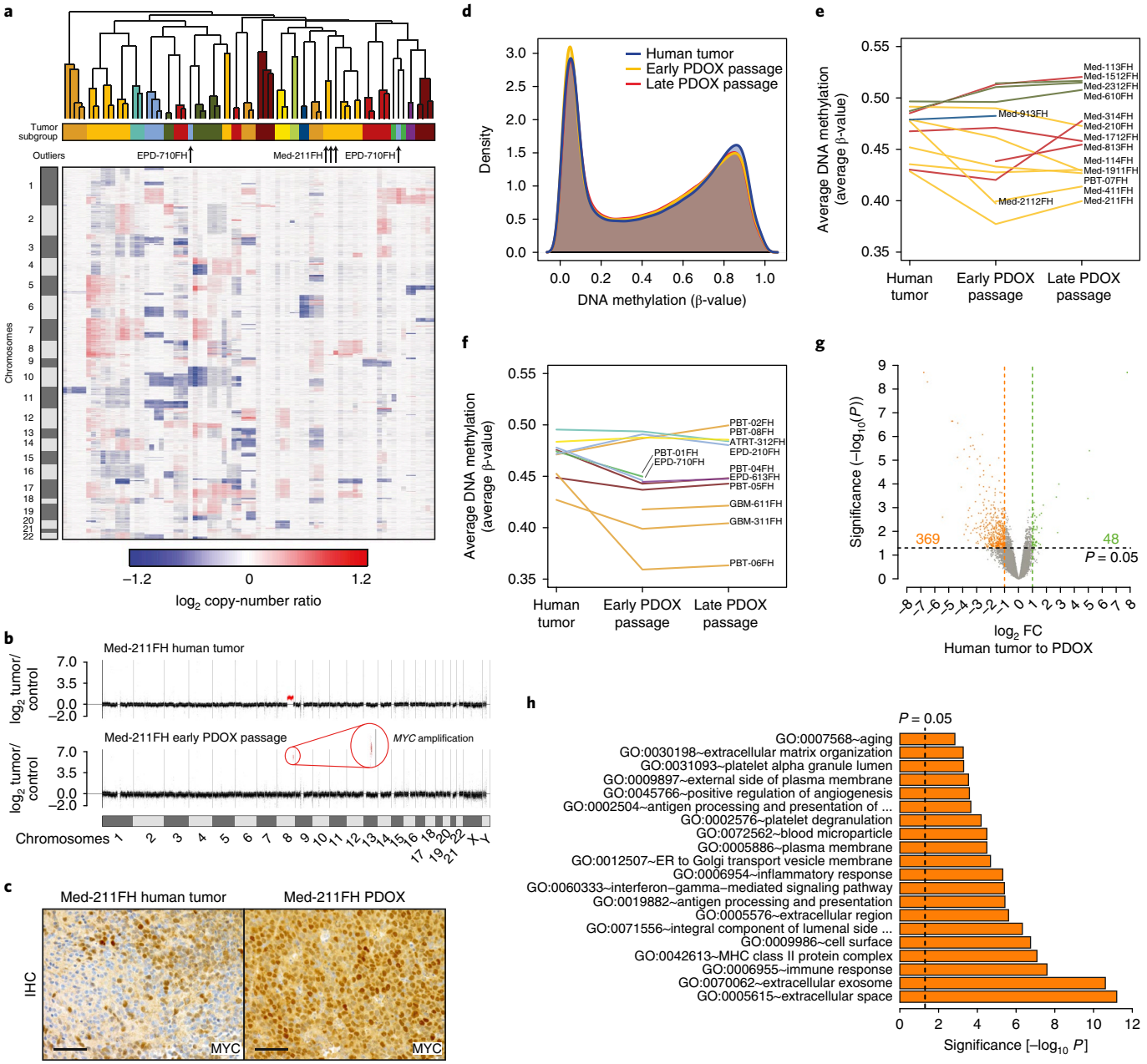

Fig. 5 | Molecular fidelity of PDOX models. a, Unsupervised hierarchical clustering of copy-number variations derived from methylation data of all PDOX models with more than one methylation profile per model. The relative intensity is depicted in the heatmap along the chromosomes (*y* axis) (red, high; blue, low). Samples are colored based on their molecular subgroup (Fig. 3). The coloring in the dendrogram highlights samples belonging to the same PDOX model. Samples not clustering with the other samples from their model are highlighted. **b**, Copy-number profile of human tumor and early PDOX passage of Med-211FH. Data were generated using binned whole-genome sequencing reads normalized to the total number of reads and normalizing it back to control tissue (log_2 tumor/control). Regions of interest are highlighted in red. **c**, Immunohistochemistry of human tumor and PDOX Med-211FH identified a small population of high MYC-expressing cells in the human tumor and high MYC expression in all PDOX cells. Scale bar, 50 µm. $n=1$ PDOX and human tumor pair. **d**, β-value density plot showing mean DNA methylation distribution of 450k methylation array probes in paired human tumors, early PDOX, and late PDOX. $n=18$ biologically independent trios. **e**,**f**, Average DNA methylation levels (average β-value) of individual PDOX models over time. The PDOX models are colored according to their tumor subgroup (Fig. 3). **g**, Average expression level changes from human tumor to PDOX. Significantly differentially expressed probes are highlighted in orange (downregulated in PDOX, total count provided: 462 probes; 369 genes) and green (upregulated in PDOX, total count provided: 54 probes; 48 genes) ($P<0.05$ and $log_2FC>1$). $n=15$ biologically independent pairs. Two-sided moderated paired *t*-test with limma. **h**, DAVID gene enrichment analysis (GO term BP and CC) of significantly higher expressed genes in PDOX passages. The top 20 GO terms ranked by *P* value are depicted. The dashed line illustrates the *P* value cutoff 0.05. Full list available in Supplementary Table 5. $n=369$ genes. Modified Fisher Exact test corrected by Benjamini method for multiple testing in DAVID.

Unsupervised hierarchical clustering of copy-number profiles of PDOX tumors, generated from DNA methylation arrays, showed that PDOX models almost always cluster next to their primary tumor and other passages (Fig. 5a), indicating that the overall copy-number landscape was preserved between human tumors and PDOX models. Still, we detected several minor

changes between primary human tumor and PDOX, which suggest continuous evolution of the tumor on serially passaging in mice. We observed two exceptions with more pronounced changes between human tumor and PDOX: EPD-710FH gained chromosome 1q in the PDOX, and Med-211FH transformed a gain of chromosome 8 into a *MYC* amplification in the PDOX model (Fig. 5b). Both acquired lesions are associated with a worse prognosis in the respective entity[31,34] and therefore point toward clonal outgrowth of an aggressive subclonal population of the human tumor in the PDOX. Indeed, when we analyzed the human tumor of Med-211FH on a single cell level with immunohistochemistry, we could detect that only a minority of the tumor cells expressed MYC at high levels, while in the PDOX model all cells were positive for MYC, consistent with selection for the *MYC*-amplified clone (Fig. 5c). Overall, except for a subclonal *TCF4* mutation in a medulloblastoma, all 'driver events' (39) were maintained in our cohort of 19 PDOX with matching human tumors, while two new driver events emerged in the PDOX, potentially due to clonal expansion (Supplementary Fig. 5i). 'Driver events' observed in early PDOX passages were also always maintained in late PDOX passages (PDOX lines: 23, mutations: 48/48, other alterations: 26/26) (Supplementary Table 4).

Interestingly, analysis of the mutational landscape of our PDOX cohort compared with mutational frequencies in the respective tumor populations revealed a strong bias for PDOX models of high-risk patients across multiple entities. For example, 50% (2/4) of our MB-SHH models harbor *MYCN* and *GLI2* amplifications (population: *MYCN* 7%, *GLI2* 9%)[27], 71% (5/7) of our MB-Group3 models harbor a *MYC* amplification (population: 17%)[27], and both of our EPN-PFA models carry a gain of chromosome 1q (population: 25%)[11] (Fig. 4). These high-risk models also grew faster in mice than did other models for example, MB high-risk (P0, mean latency 73 days) versus average risk (P0, mean latency 175 days, $P = 5.3 \times 10^{-5}$) (Supplementary Table 1).

Molecular fidelity of PDOX models. To analyze the fidelity of the PDOX models in relation to their matching human counterpart on a genomic scale, we compared the average DNA methylation levels of paired human tumors, early PDOX passages, and late PDOX passages. In general, global DNA methylation levels were highly similar between human tumors and PDOX models (Fig. 5d). Average correlation of average DNA methylation between human tumor, early PDOX passage, and late PDOX passage showed a correlation coefficient of higher than 0.99 and pairwise comparisons detected less than 0.2% differentially methylated probes (human tumor-early passage: 215 (0.047%); human tumor-late passage: 517 (0.11%)) (Supplementary Fig. 6a–e). Tracking the overall DNA methylation per model, we observed that some tumors acquired hypomethylation over time, while others gained overall methylation (Fig. 5e,f), which probably points to individual continuous evolution per model rather than any systematic changes introduced by the murine environment.

Pairwise comparison of PDOX and human tumor samples on the gene expression level ($n = 15$) also showed a very high correlation (Pearson's coefficient 0.99) (Supplementary Fig. 6f) and only identified 369 genes with significantly reduced expression and 48 with increased expression in the PDOX samples, compared with the corresponding patient samples (Fig. 5g and Supplementary Table 5). DAVID pathway enrichment analysis identified that genes with reduced expression were mostly associated with human stroma, which is replaced by murine stroma in the mouse (Fig. 5h and Supplementary Table 5). Genes with increased expression in the PDOX models were mostly associated with cell cycle activation, possibly reflecting either increased cell purity in the mouse or some selection for more rapidly dividing cells (Supplementary Fig. 6g and Supplementary Table 5).

We concluded that all PDOX models faithfully recapitulate the human tumors from which they are derived and remain relatively stable when being passaged in mice. With the exception of rare events of clonal outgrowth, only minor changes were observed between human tumors and PDOX models or between different passages of PDOX models, probably reflecting a natural continuous evolution of cancer as well as species-specific change of the microenvironment.

Therapeutic response confirms genetic vulnerability predicted by molecular analysis. To assess whether genomic vulnerabilities identified by molecular analysis could be translated into potential therapeutic targets, two comparisons between predicted sensitive and resistant tumor models were made. First, two PDOX models (PBT-04FH and PBT-05FH), both molecularly classified as models representing HGG-MYCN tumors and both harboring a *MYCN* amplification, but differentiating by *EGFR* amplification and overexpression in only one model (PBT-05FH), were evaluated for sensitivity to EGFR kinase inhibition with erlotinib. PBT-04FH (no *EGFR* amplification) and PBT-05FH (*EGFR* amplification) tumors were treated with erlotinib at 2 mg per mouse daily by oral gavage. Mice transplanted with *EGFR*-amplified PBT-05FH tumors survived significantly longer on treatment compared with the vehicle-treated control group (26 versus 6 days; $P = 0.0001$) (Fig. 6a). Treatment with erlotinib completely abolished EGFR phosphorylation in PBT-05FH (Supplementary Figs. 7a and 8a–d). In contrast, mice transplanted with the low *EGFR*-expressing tumor model PBT-04FH fared worse on erlotinib treatment, with a median survival of only 8 days compared with 17 days for the vehicle group (Fig. 6b), due to erlotinib-induced weight loss, while at the same time tumor-related weight loss was not delayed (Supplementary Fig. 7b). In a second comparison, two MB-SHH models, each with a different mutational status, were treated with the smoothened (SMO) inhibitor, vismodegib. Med-1712FH harboring a *PTCH1* mutation had an improved median survival of 16 days when treated with vismodegib, versus 10 days for the vehicle-treated cohort ($P = 0.0502$) (Fig. 6c). As expected, SHH pathway genes were downregulated in Med-1712FH after treatment with vismodegib (Supplementary Fig. 7c). In contrast, Med-813FH, driven by *MYCN* and *GLI2* amplifications, showed no improvement in median survival: 6 days with vismodegib treatment versus 8.5 days with vehicle treatment (Fig. 6d). In a similar approach, orthotopic brain tumors started with a luciferase-labeled subline of Med-1712FH were treated with the SMO inhibitor erismodegib, which also led to potent downregulation of the SHH pathway (Supplementary Fig. 7d). Following the relative luciferase signal over time, we observed a drastic response to the inhibitor while the tumors of the vehicle group progressed exponentially (Fig. 6e). Three weeks after treatment start, 86% (12/14) of the treated animals showed regression (<70% of initial signal) (Fig. 6f), highlighting the potential clinical impact of targeted therapy in pediatric neuro-oncology.

A recent publication by Pei et al. proposed to treat high-risk MB driven by *MYC* amplification with the histone deacetylase (HDAC) inhibitor panobinostat[35]. Indeed, panobinostat significantly increased survival of mice harboring Med-114FH tumors (MB-Group3, *MYC* amplification) compared with controls (29.5 versus 12 days, $P = 0.0294$) (Fig. 6g). The genetically engineered SmoA1 model of MB-SHH has also been shown previously to respond to HDAC inhibition[36,37], and we therefore evaluated panobinostat in a PDOX model representing high-risk MB-SHH patients who are not responsive to SMO inhibitors and carry *TP53* mutations and *MYCN*/*GLI2* amplifications. Mice transplanted with Med-314FH cells (MB-SHH, *TP53*, *MYCN*, *GLI2*) survived significantly longer when treated with panobinostat than vehicle controls (20 versus 9.5 days, $P = 0.0011$) (Fig. 6h). Treatments with panobinostat also led to an increase in acetylation of histone 3, confirming

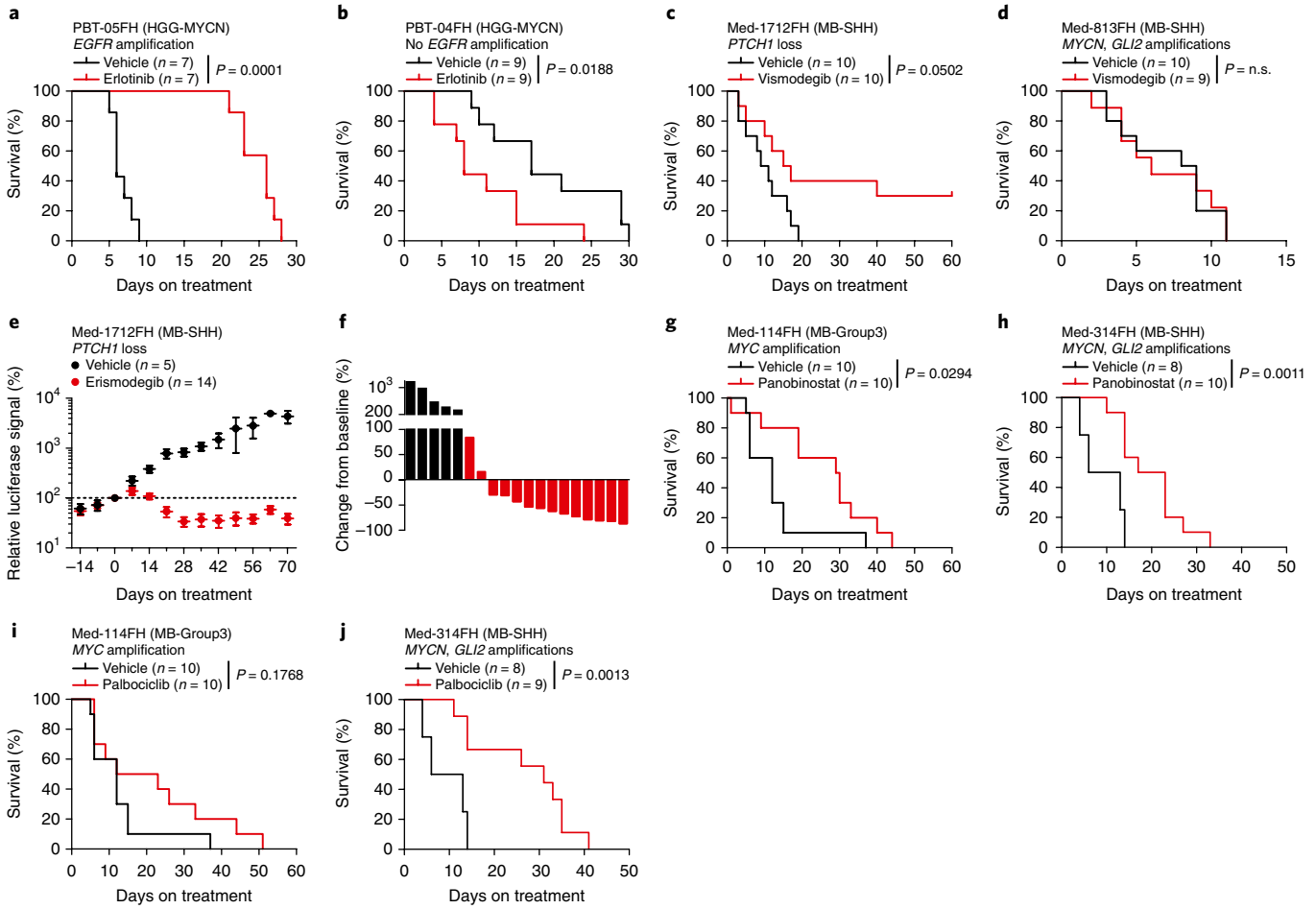

Fig. 6 | Preclinical evaluation of targeted therapeutics shows differential response to therapy based on molecular drivers. a–d, Kaplan–Meier analyses of PBT-05FH treated with erlotinib 2 mg per mouse or vehicle daily by oral gavage; $n = 7$ per group ($P = 0.0001$) (**a**), PBT-04FH treated with erlotinib 2 mg per mouse or vehicle daily by oral gavage; $n = 9$ per group ($P = 0.0188$) (**b**), Med-1712FH treated with vismodegib 1 mg per mouse daily for 5/7 days by oral gavage; $n = 10$ per group ($P = 0.0502$) (**c**), and Med-813FH treated with vismodegib 1 mg per mouse daily for 5/7 days by oral gavage; $n \geq 9$ per group ($P > 0.99$) (**d**). Two-sided log-rank (Mantel–Cox) test. **e**, Med-1712FH treated with erismodegib 30 mg kg^{-1}or vehicle daily for 5/7 days by oral gavage. Average relative luciferase signal normalized to luciferase signal at treatment start over the period of the study (vehicle, black; erismodegib, red). Mean ± s.e.m.. **f**, Waterfall plot at 3 weeks treatment with erismodegib or vehicle showing the relative change from baseline of treatment of start of the luciferase signal per individual animal. Each bar represents one mouse that is colored based on its treatment group (vehicle, black; erismodegib, red). **g–j**, Kaplan–Meier analysis of Med-114FH treated with panobinostat 20 mg kg^{-1}daily for 5/7 days by intraperitoneal injection; $n = 10$ per group ($P = 0.0294$) (**g**), Med-314FH treated with panobinostat 10 mg kg^{-1} or vehicle daily for 5/7 days by intraperitoneal injection; $n \geq 8$ per group ($P = 0.0011$) (**h**), Med-114FH treated with palbociclib 120 mg kg^{-1} or vehicle daily for 5/7 days by oral gavage; $n = 10$ per group ($P = 0.1768$) (**i**), and Med-314FH treated with palbociclib 100 mg kg^{-1} or vehicle daily for 5/7 days by oral gavage; $n \geq 8$ per group ($P = 0.0013$) (**j**). Two-sided logrank (Mantel–Cox) test.

the inhibition of HDACs (Supplementary Figs. 7e and 8e). Another potential novel treatment option for medulloblastoma are CDK4/6 inhibitors such as palbociclib[38]. Treatment with palbociclib resulted in inhibition of retinoblastoma phosphorylation (Supplementary Figs. 7f and 8f,g), a significant survival advantage for Med-314FH-bearing animals (median survival: 31 versus 9.5 days, $P = 0.0013$) (Fig. 6i), and an improved median survival for Med-114FH-bearing mice (17.5 days versus 12 days, $P = 0.1768$) (Fig. 6j).

A resource for the community. Due to the rarity of pediatric brain tumors and the multitude of different entities, subgroups, and additional inter-tumoral heterogeneity, it is critical that the scientific community is able to study this repertoire of preclinical models adequately representing the entire spectrum of pediatric brain tumors. To make our PDOX resource available to the scientific community, we share our PDOX models and cell lines through the brain tumor resource lab website (http://www.btrl.org), which facilitates access to all models described here, as well as additional models currently undergoing molecular characterization. The molecular and histopathological data are available and can be explored through the R2 PDX Explorer (http://www.r2platform.com/pdxexplorer), allowing scientists all over the world to find the right PDOX line for a particular scientific question (Supplementary Fig. 9). A summary of the essential information for each PDOX or cell line model is available online in the PDX Explorer and at the brain tumor resource lab website (see example, Supplementary Fig. 10). Furthermore, 44 additional external PDOX lines are listed on both websites, including their molecular subgroups and contact details of the responsible principal investigator.

Discussion

Faithful model systems are critical tools for cancer research to facilitate the study of tumor biology and anticancer therapy in vitro and in vivo. The 30 PDOX models and three independent cell lines

described here are each representatives of rare molecular subgroups of human disease, and collectively comprise a good representation of malignant pediatric brain tumors. PDOX models allow for continued interaction between tumor cells and the microenvironment of the central nervous system, which appears to reduce molecular adaptation to artificial growth conditions observed in many cancer cell lines[39,40]. The molecular characterization of these models, including histology, methylation status, gene expression, and DNA sequencing, indicates that these models are highly similar to the tumors they are derived from and therefore provide an unprecedented resource to study pediatric brain tumors and cancer pathways in a more endogenous setting. Many of the models described here are derived from human tumors for which there are currently no preclinical in vivo models available, including, but not limited to, non-*MYC*-amplified MB-Group3, *KBTBD4*-mutant MB, *PRDM6*-driven MB-Group4, hypermutated *HGG*, HGG-MYCN, different subgroups of ATRT, pineoblastoma, and EPN-PFA. Overall, this is the first description of a molecularly well-annotated cohort of PDOX models for pediatric brain tumors that is available to the entire scientific community.

The importance of evaluating diverse and clinically relevant preclinical tumor models within a single disease can be exemplified in MB, the most common embryonal brain tumor in children. MB are notoriously difficult to grow in cell culture conditions. However, in our hands 15 of 41 different MB patient samples successfully engrafted as PDOX in mice. The PDOX models of MB presented here represent all molecular subgroups that have been described so far. As expected, we established a disproportionate number of models representing the most aggressive and deadly subgroups of disease, including Group 3 *MYC*-amplified tumors and SHH pathway tumors with *TP53* mutation. Both subgroups represent the MB tumors with the worst prognosis, and these patients are most desperately in need of novel therapeutic options[41].

Selection for high-risk tumors also holds true in other entities, for example EPN-PFA, EPN-RELA, HGG-K27M or HGG-MYCN, and has also been described in PDX cohorts of adult cancers[42]. In the example of HGG-MYCN, we showed that in-depth molecular profiling of the PDOX models can pave the way for novel therapeutic strategies. In the context of this very aggressive tumor subgroup, with a median overall survival of less than 12 months[25], an *EGFR* amplification predicted the response to erlotinib in one PDOX pair. Intriguingly, in a molecularly stratified cohort of 36 HGG-MYCN patients, 25% harbor an *EGFR* amplification[25], which makes our finding applicable to a defined patient subpopulation. The failure of erlotinib in clinical trials for adult HGG highlights that this concept needs to be validated in more independent PDOX models and needs to be developed further into a combination therapy[43–45]. However, due to the rarity of the disease, our repertoire of PDOX is currently underpowered to systematically answer this question for pediatric patients.

PDOX models offer a number of distinct advantages over other preclinical models. Although the stroma in PDOX mouse models is of non-human origin, the composition of the tumor microenvironment in most cases compares well with the structure in human tumors[46]. PDOX tumors are never exposed to cell culture conditions, and can be seeded into P0 mice within hours of surgical resection. This technique provides an excellent opportunity to develop models for diseases without known molecular drivers. Once practiced, orthotopic xenograft implantation can be an efficient process taking only a few minutes per mouse to perform. We were able to create PDOX tumor lines from 30% of the human tumors we implanted, a below-average rate compared with other pediatric or adult cancers[42,47], irrespective of whether material was implanted on the same day as the operation or shipped overnight. Once beyond the earliest passages, the time to an observable tumor was reliably less than three months, with few exceptions in slower growing molecular subgroups (for example MB-Group4 or PB). A brain tumor resected from a single mouse regularly provides enough cells to seed new tumors in over 20 naïve mice, making it possible to perform large-scale studies with a small starting group and in a reasonable amount of time. PDOXs provides a model system for growing human tumor cells with minimized exposure to foreign agents in a microenvironment that resembles the host.

Generally, a high level of genomic stability between PDOX models and their matching human tumors was observed, but there were a few exceptions: for instance, the *MYC* amplification in the Med-211FH model or the 1q gain in the EPD-710FH model probably appeared due to a clonal selection process of minor cell populations of the human tumor during progression of a xenograft tumor, as previously reported in other disease models such as breast cancer[17,48]. It is highly likely that this selection process reflects normal tumor evolution, as, for example, *MYC* amplifications are more common in relapses than in primary MB[49]. To gain further insights into these processes, additional in-depth comparative genomic approaches will be necessary, which would, however, require proper germline controls that were lacking for this study. Furthermore, researchers should be cautioned about the risk of development of mouse tumors at the site of orthotopic implantation. Standard comparative histologic evaluation of PDOX passages by an experienced pathologist, as well as STR analyses, should be considered as necessary and sufficient methods to differentiate human from mouse tumors.

In summary, we have established and molecularly characterized 30 unique PDOX models and three new cell lines of pediatric brain tumors that provide a valuable resource to assess new therapeutic approaches and to better understand the basis for therapeutic sensitivity or resistance, particularly in rare tumor types where fundamental disease etiology remains either elusive or where no successful therapy options exist. In the era of precision medicine, access to a large repertoire of molecularly well-characterized model systems is essential to test new, targeted treatment strategies. By sharing the models and the molecular data, we want to pave the way for large, collaborative preclinical approaches in the future. The PDX Explorer as an interactive online platform will facilitate this endeavor as an expandable central hub for (pediatric brain tumor) PDOX. In addition, the paucity of potentially confounding genomic variations in pediatric brain tumors may create opportunities to address hypotheses focused on key drivers and oncogenic pathways that are relevant in many other pediatric and adult cancers.

Online content

Any methods, additional references, Nature Research reporting summaries, source data, statements of data availability and associated accession codes are available at https://doi.org/10.1038/s41591-018-0207-3.

Received: 12 July 2017; Accepted: 14 August 2018;
Published online: 22 October 2018

References

1. Taylor, M. D. et al. Molecular subgroups of medulloblastoma: the current consensus. *Acta Neuropathol.* **123**, 465–472 (2012).
2. Johann, P. D. et al. Atypical teratoid/rhabdoid tumors are comprised of three epigenetic subgroups with distinct enhancer landscapes. *Cancer Cell* **29**, 379–393 (2016).
3. Torchia, J. et al. Integrated (epi)-genomic analyses identify subgroup-specific therapeutic targets in CNS rhabdoid tumors. *Cancer Cell* **30**, 891–908 (2016).
4. Sturm, D. et al. Hotspot mutations in H3F3A and IDH1 define distinct epigenetic and biological subgroups of glioblastoma. *Cancer Cell* **22**, 425–437 (2012).
5. Johnson, R. A. et al. Cross-species genomics matches driver mutations and cell compartments to model ependymoma. *Nature* **466**, 632–636 (2010).
6. Witt, H. et al. Delineation of two clinically and molecularly distinct subgroups of posterior fossa ependymoma. *Cancer Cell* **20**, 143–157 (2011).

7. Gajjar, A., Pfister, S. M., Taylor, M. D. & Gilbertson, R. J. Molecular insights into pediatric brain tumors have the potential to transform therapy. *Clin. Cancer Res.* **20**, 5630–5640 (2014).
8. Capper, D. et al. DNA methylation-based classification of central nervous system tumours. *Nature* **555**, 469–474 (2018).
9. Louis, D. N. et al. The2016 World Health Organization classification of tumors of the central nervous system: a summary. *Acta Neuropathol.* **131**, 803–820 (2016).
10. Pajtler, K. W. et al. The current consensus on the clinical management of intracranial ependymoma and its distinct molecular variants. *Acta Neuropathol.* **133**, 5–12 (2017).
11. Pajtler, K. W. et al. Molecular classification of ependymal tumors across all CNS compartments, histopathological grades, and age groups. *Cancer Cell* **27**, 728–743 (2015).
12. Shou, Y. et al. A five-gene hedgehog signature developed as a patient preselection tool for hedgehog inhibitor therapy in medulloblastoma. *Clin. Cancer Res.* **21**, 585–593 (2015).
13. Gilbertson, R. J. Brain tumors provide new clues to the source of cancer stem cells: does oncology recapitulate ontogeny? *Cell Cycle* **5**, 135–137 (2006).
14. Packer, R. J. et al. Phase III study of craniospinal radiation therapy followed by adjuvant chemotherapy for newly diagnosed average-risk medulloblastoma. *J Clin. Oncol.* **24**, 4202–4208 (2006).
15. Gao, H. et al. High-throughput screening using patient-derived tumor xenografts to predict clinical trial drug response. *Nat. Med.* **21**, 1318–1325 (2015).
16. Townsend, E. C. et al. The public repository of xenografts enables discovery and randomized phase II-like trials in mice. *Cancer Cell* **30**, 183 (2016).
17. Bruna, A. et al. A biobank of breast cancer explants with preserved intra-tumor heterogeneity to screen anticancer compounds. *Cell* **167**, 260–274.e222 (2016).
18. Houghton, P. J. et al. The pediatric preclinical testing program: description of models and early testing results. *Pediatr. Blood Cancer* **49**, 928–940 (2007).
19. Zhao, X. et al. Global gene expression profiling confirms the molecular fidelity of primary tumor-based orthotopic xenograft mouse models of medulloblastoma. *Neuro. Oncol.* **14**, 574–583 (2012).
20. Grasso, C. S. et al. Functionally defined therapeutic targets in diffuse intrinsic pontine glioma. *Nat. Med.* **21**, 827 (2015).
21. Goldenberg, D. M. & Pavia, R. A. In vivo horizontal oncogenesis by a human tumor in nude mice. *Proc. Natl Acad. Sci. USA* **79**, 2389–2392 (1982).
22. Triviai, I. et al. Endogenous retrovirus induces leukemia in a xenograft mouse model for primary myelofibrosis. *Proc.Natl Acad. Sci. USA* **111**, 8595–8600 (2014).
23. Hovestadt, V. et al. Decoding the regulatory landscape of medulloblastoma using DNA methylation sequencing. *Nature* **510**, 537–541 (2014).
24. Sturm, D. et al. New brain tumor entities emerge from molecular classification of CNS-PNETs. *Cell* **164**, 1060–1072 (2016).
25. Korshunov, A. et al. H3-/IDH-wild type pediatric glioblastoma is comprised of molecularly and prognostically distinct subtypes with associated oncogenic drivers. *Acta Neuropathol.* **134**, 507–516 (2017).
26. Mackay, A. et al. Integrated molecular meta-analysis of 1,000 pediatric high-grade and diffuse intrinsic pontine glioma. *Cancer Cell* **32**, 520–537 (2017). e525.
27. Northcott, P. A. et al. The whole-genome landscape of medulloblastoma subtypes. *Nature* **547**, 311–317 (2017).
28. Callari, M. et al. Computational approach to discriminate human and mouse sequences in patient-derived tumour xenografts. *BMC Genomics* **19**, 19 (2018).
29. Northcott, P. A. et al. Enhancer hijacking activates GFI1 family oncogenes in medulloblastoma. *Nature* **511**, 428–434 (2014).
30. Pajtler, K. W. et al. Molecular heterogeneity and CXorf67 alterations in posterior fossa group A (PFA) ependymomas. *Acta Neuropathol.* **136**, 211–226 (2018).
31. Kilday, J. P. et al. Copy number gain of 1q25 predicts poor progression-free survival for pediatric intracranial ependymomas and enables patient risk stratification: a prospective European clinical trial cohort analysis on behalf of the Children's Cancer Leukaemia Group (CCLG), Societe Francaise d'Oncologie Pediatrique (SFOP), and International Society for Pediatric Oncology (SIOP). *Clin. Cancer Res.* **18**, 2001–2011 (2012).
32. Parker, M. et al. C11orf95-RELA fusions drive oncogenic NF-kappaB signalling in ependymoma. *Nature* **506**, 451–455 (2014).
33. Biegel, J. A. Molecular genetics of atypical teratoid/rhabdoid tumor. *Neurosurg. Focus* **20**, E11 (2006).
34. Shih, D. J. et al. Cytogenetic prognostication within medulloblastoma subgroups. *J. Clin. Oncol.* **32**, 886–896 (2014).
35. Pei, Y. et al. HDAC and PI3K antagonists cooperate to inhibit growth of MYC-driven medulloblastoma. *Cancer Cell* **29**, 311–323 (2016).
36. Lee, S. J. et al. Sonic hedgehog-induced histone deacetylase activation is required for cerebellar granule precursor hyperplasia in medulloblastoma. *PLoS ONE.* **8**, e71455 (2013).
37. Spiller, S. E., Ditzler, S. H., Pullar, B. J. & Olson, J. M. Response of preclinical medulloblastoma models to combination therapy with 13-cis retinoic acid and suberoylanilide hydroxamic acid (SAHA). *J. Neurooncol.* **87**, 133–141 (2008).
38. Cook Sangar, M. L. et al. Inhibition of CDK4/6 by palbociclib significantly extends survival in medulloblastoma patient-derived xenograft mouse models. *Clin. Cancer Res.* **23**, 5802–5813 (2017).
39. Varley, K. E. et al. Dynamic DNA methylation across diverse human cell lines and tissues. *Genome Res.* **23**, 555–567 (2013).
40. Goodspeed, A., Heiser, L. M., Gray, J. W. & Costello, J. C. Tumor-derived cell lines as molecular models of cancer pharmacogenomics. *Mol. Cancer Res.* **14**, 3–13 (2016).
41. Ramaswamy, V. et al. Medulloblastoma subgroup-specific outcomes in irradiated children: who are the true high-risk patients? *Neuro Oncol.* **18**, 291–297 (2016).
42. Hidalgo, M. et al. Patient-derived xenograft models: an emerging platform for translational cancer research. *Cancer Discov.* **4**, 998–1013 (2014).
43. Peereboom, D. M. et al. Phase II trial of erlotinib with temozolomide and radiation in patients with newly diagnosed glioblastoma multiforme. *J. Neurooncol.* **98**, 93–99 (2010).
44. Wen, P. Y. et al. Phase I/II study of erlotinib and temsirolimus for patients with recurrent malignant gliomas: North American Brain Tumor Consortium trial 04-02. *Neuro Oncol.* **16**, 567–578 (2014).
45. Raizer, J. J. et al. A phase II study of bevacizumab and erlotinib after radiation and temozolomide in MGMT unmethylated GBM patients. *J. Neurooncol.* **126**, 185–192 (2016).
46. Sflomos, G. et al. A preclinical model for ERα-positive breast cancer points to the epithelial microenvironment as determinant of luminal phenotype and hormone response. *Cancer Cell* **29**, 407–422 (2016).
47. Stewart, E. et al. Orthotopic patient-derived xenografts of paediatric solid tumours. *Nature* **549**, 96–100 (2017).
48. Eirew, P. et al. Dynamics of genomic clones in breast cancer patient xenografts at single-cell resolution. *Nature* **518**, 422–426 (2015).
49. Hill, R. M. et al. Combined MYC and P53 defects emerge at medulloblastoma relapse and define rapidly progressive, therapeutically targetable disease. *Cancer Cell* **27**, 72–84 (2015).

Acknowledgements

We are grateful to the patients and families who consented to provide tissue to generate these resources. We thank A. Richards, M. Merrill, D. Acorn, M. Biery, A. Wittmann, and L. Sieber for experimental contributions. We thank the DKFZ Genomics and Proteomics Core Facility, DKFZ Heidelberg, Germany, and the AMC Department of Oncogenomics, Amsterdam, The Netherlands, for performing high-throughput sequencing and microarray analyses to a very high standard. We also thank the DKFZ data management group, especially I. Scholz, for their excellent support in processing the sequencing data, and Z. Gu for the defuse pipeline. We thank X.-N. Li, R. J. Wechsler-Reya, and T. Milde for allowing us to list their PDOX lines on our websites. This work was supported by NIH 1U10CA180886-01 (J.M.O.), NIH 1R01CA155360 (J.M.O.), NIH R01 CA114567 (J.M.O.), the Seattle Run of Hope, the Seattle Children's Brain Tumor Research Endowment, the Dutch Cancer Foundations KWF (2010-4713) (M.K.) and KIKA (90) (M.K.), Deutsche Krebshilfe (111537) (S.M.P., M.K.), BMBF (01KT1605) (S.M.P., M.K.), IMI-JU ITCC-P4 (116064) (D.T.W.J., J.K., S.M.P., M.K.), and the Helmholtz International Graduate School for Cancer Research (S.B.).

Author contributions

S.B., S.E.S.L., S.N.G., M.W.N., H.S.-C, E.J.G., B.C., A.D.S., K.L.B., N.L.M., F.P., B.S., A.K., K.D.P., J.D., S.H., and S.D. performed and/or coordinated the experimental work. S.B., S.E.S.L., S.N.G., M.W.N., H.S.-C., E.J.G, B.C., A.D.S., K.L.B., V.H., A.K., G.P.B., P.A.N., K.D.P., S.H., S.D., P.L., L.C., D.T.W.J., J.K., and M.K. performed data analysis and interpretation. S.B., S.E.S.L., S.N.G., S.M.P., M.K., and J.M.O. provided project leadership. S.B., S.E.S.L., S.N.G., S.M.P., M.K., and J.M.O. prepared the initial manuscript and figures. All authors contributed to the critical review of the manuscript.

Competing interests

The authors declare no competing interests.

Additional information

Supplementary information is available for this paper at https://doi.org/10.1038/s41591-018-0207-3.

Reprints and permissions information is available at www.nature.com/reprints.

Correspondence and requests for materials should be addressed to S.M.P. or M.K. or J.M.O.

Publisher's note: Springer Nature remains neutral with regard to jurisdictional claims in published maps and institutional affiliations.

Methods

Patient samples. Brain tumor tissue was obtained through the Children's Oncology Group brain tumor biology study ACNS02B3 (NCT00919750). The ACNS02B3 study was approved by the Institutional Review Board of each participating Children's Oncology Group institution. Informed consent of the parent or legal guardian, and patient assent when appropriate, was obtained according to institutional regulatory standards before surgery or autopsy. Fresh tumor tissue for research was selected by the pathologist or surgeon at each treating institution after clinical diagnostic tissue was obtained. Approximately 100 mg of fresh tissue was placed in a 15-ml polypropylene tube with DMEM-F12. Samples from Seattle Children's were transferred on wet ice and processed within hours of patient surgery. Other samples from across the United States and Canada were shipped overnight on wet ice and typically processed within 24 h of surgery. Patient age, gender, and preliminary diagnosis were provided at the time of tissue shipment. Final institutional pathologic diagnosis was provided once available. Patient tumor tissue was triturated with an 18 G needle, to yield a single cell suspension. The resulting suspension of cells was filtered through a nylon mesh 100-µm sterile cell strainer (Fisher Scientific, 22363549) and concentrated to 50,000 cells μl^{-1} in serum-free DMEM in preparation for intracranial xenograft into five recipient mice. Cells from the remaining sample (2–3 million) were plated for growth in tissue culture. Up to 1 million remaining cells were used for pathogen testing.

Xenograft development. Xenograft of tumor cell suspension was carried out in immune-compromised mice (Nod-scid IL2Rgamma^{null} or athymic nude) immediately following processing. Female athymic Nu/Nu mice were purchased (Jackson Laboratories or Harlan Laboratories; now Envigo Laboratories). NSG mice were obtained from the laboratory breeding colony, established by breeding pairs purchased (Jackson Laboratories). All mice were maintained in accordance with the National Institutes of Health (NIH) *Guide for the Care and Use of Laboratory Animals* with approval from the Fred Hutchinson Cancer Research Center Institutional Animal Care and Use Committee (IR no. 1457).

Analgesia was administered by subcutaneous buprenorphine injection approximately one hour before beginning the procedure. Mice were anesthetized using inhaled isoflurane. Establishment of anesthesia was determined by monitoring respiratory rate and toe pinch reflex. The surgical site was prepared by shaving the fur between the ears and partially down the neck. Puralube Vet Ointment sterile ocular lubricant (MWI Veterinary Supply, 027505) was applied to both eyes, and a 1-ml subcutaneous bolus of sterile saline (Braintree Scientific, SYS 5-5) was administered. Surgery was performed in a clean surgical field. The surgical site was cleaned by scrubbing the skin with a cotton swab impregnated with betadine (Santa Cruz Biotechnology, sc-359867) followed by a sterile 70% ethanol wipe (Fisher Scientific, 22-363-750). An incision of ~1 cm was made along the mediolateral line starting between the ears and ending near the back of the skull using a disposable scalpel (Exel Int., 29550). Using cotton-tipped applicators (Puritan, 25-806 10WC) the skull was exposed and cleaned of any minor connective tissues or blood. Once the area was clean, a handheld microdrill (Cell Point Scientific, Ideal Microdrill, 67-1000) with a 0.9 mm burr (Fine Scientific Tools, 19007-09) was used to create a burr hole into the cortex or cerebellum, corresponding to the in situ location of the source tissue. Cell suspension (2 µl; 100,000 cells) was deposited into the intracranial space by inserting a 10 µl Rainin Pipette-Lite fitted with a 2–10 µl ART tips barrier non-filtered pipette tip (Thermo Scientific, 2139). A small piece of surgical foam (Pfizer Injectables, 09-0396-05) was placed onto the burr hole before pulling the incision closed and bonding the skin together with veterinary-grade surgical glue (3M, Vetbond). Following closure of the incision, mice were removed from isofluorane and transferred to a clean recovery cage placed on a heat mat for the duration of recovery. After recovery mice were returned to their home cage.

Mice implanted with patient-derived tumor cells were monitored regularly for signs of tumor formation, which can include distension of the calvarium, head tilt, reduced feeding, weight loss, dehydration, hunched posture, eye irritation, or poor grooming habits. On observation of symptoms mice were euthanized and tumor presence was confirmed visually during tissue resection. Tumor tissue was formalin-fixed, cryopreserved, and processed for serial transplantation into a new cohort of mice.

Tissue culture. The growth conditions for our primary human pediatric cancer cell lines are a modification of Lee et al.[50]. Cell lines were grown in NeuroCult NS-A Basal Medium (Human) plus NeuroCult NS-A Proliferation Supplements (Human) (Stem Cell Technologies, 05750 and 05753). The media also contained a final concentration of 20 µg ml^{-1} each of epidermal growth factor and fibroblast growth factor (Preprotech, AF-100-15 and 315-09). Before seeding cells, Petri dishes or flasks were coated with laminin from Engelbreth-Holm-Swarm murine sarcoma basement membrane (Sigma-Aldrich, L2020). A solution of 1 mg ml^{-1} laminin in Dulbecco's phosphate-buffered saline without calcium chloride, without magnesium chloride (ThermoFisher Scientific, 14190250) was used to cover the bottom of the tissue culture-treated dish or flask at 37 °C for 1–3 h.

Tumor pathology. A pediatric pathologist (B.C.) evaluated PDOX tumors in comparison with primary human tumor for all samples obtained from Seattle Children's and Children's Oncology Group samples when available. Immunohistochemistry analyses were performed on 4 µm paraffin sections of the whole-brain mounts stained using an automated Ventana Benchmark Stainer. Sections were incubated with primary antibodies (brand/catalog number/lot number/dilution): TP53 (Proteintech/10442-1-AP/1/1:50), PDGFR-a (Santa Cruz Biotechnology/Sc-338/A2811/1:100), Olig 2 (Immuno-Biological Laborat ories/18953/1B-327/1:250), LIN28A (Cell Signaling Technologies/3695/2/1:50), GFAP (DAKO/M0761/00083681/1:400), Ki-67 (DAKO/M7240/00090216/1:100), INI-1 (BD Biosciences/612110/23247/1:300), EGFR (Invitrogen/280005/7877 70A/1:100), C-MYC (Thermo Scientific/MAI-980/OA179819 /1:200), N-MYC (Novus Biologicals/23960002/T00308A1/1:500), Synaptophysin (Abcam/ab32127/ GR312544-10/1:300), Beta-Catenin (Abcam/ab16051/GR3185177-1/1:200), and GAB-1 (Merck Millipore/06-579/2942435/1:800 (with a diluent containing Casein (Roche, 760-219). All antibodies were diluted in phosphate-buffered solution. Slides were incubated with biotinylated secondary antibodies, followed by incubation with the streptavidin and biotinylated peroxidase complex, both from the ultraView Universal DAB Detection Kit (Ventana Medical Systems, 760-500). Sections were counterstained with hematoxylin and mounted.

DNA and RNA isolation. Total RNA extraction was performed from snap-frozen tumor tissues using TRIzol (Invitrogen), the Qiagen miRNeasy Mini Kit (Qiagen), and analyzed on an Agilent Bioanalyser (Agilent Technologies) for quality assessment. Only samples with an RNA integrity number (RIN) > 6.0 and no evidence of ribosomal degradation were analyzed for gene expression. Genomic DNA was isolated using Qiagen DNeasy Blood & Tissue Kit (Qiagen) and used for methylation and sequencing analysis.

Gene expression array analysis. PDOX samples with sufficient quantity and quality of RNA were analyzed on the Affymetrix GeneChip Human Genome U133 Plus 2.0 Array at the Microarray Department, University of Amsterdam, The Netherlands. Sample library preparation, hybridization, and quality control were performed according to protocols recommended by the manufacturer. The MAS5.0 algorithm of the GCOS program (Affymetrix Inc) was used for normalization of expression data. Detection *P* values were assigned to each probe set using the MAS5.0 algorithm. Quality of the arrays was ensured by inspection of the beta-actin and GAPDH 5′–3′ ratios as well as the percentage of present calls generated by MAS5.0. Data were analyzed using R2 (http://R2.amc.nl)[51].

Differentially expressed genes were estimated with linear models using the limma package in R[52]. RMA normalization was performed with the simpleaffy (v. 2.46) package in R[53]. Only genes that were expressed in at least one sample were considered for the analysis (>100 intensity). Differential expression was calculated with a moderated paired *t*-test using limma (v. 3.6.29)[52] and *P* values were corrected for multiple testing with the Bonferroni method ($P > 0.05$). Significant genes, which change more than twofold between groups, were used for the follow-up analysis. DAVID 6.7 (https://david-d.ncifcrf.gov/) was used for pathway enrichment analysis using the GOTERM_BP_DIRECT and GOTERM_ CC_DIRECT gene ontology annotations[54,55].

DNA methylation array analysis. Whole-genome DNA methylation data for 81 samples presented in this study were generated from fresh frozen and formalin-fixed, paraffin-embedded material (Supplementary Table 3), using Illumina Infinium 450k Methylation BeadChip Arrays (450k arrays). Methylation profiling was performed according to the manufacturer's instructions at the DKFZ Genomics and Proteomics Core Facility, Heidelberg, Germany. All analyses were performed in R version 3.3.0 (Development Core Team, 2016). Downstream analyses as described in Hovestadt et al.[56] were performed in R using β-values. Reference cases of primary human tumors for subgrouping were taken from various previous publications as indicated in Supplementary Table 3. Normalization and generation of beta values was performed as described in Sturm et al.[24].

The following filters were applied to filter out probes that yield inaccurate methylation levels: removal of probes targeting the X and Y chromosomes ($n = 11{,}551$), removal of probes containing a single-nucleotide polymorphism (dbSNP132 Common) or the following base for type I probes ($n = 7{,}998$), and probes not mapping uniquely to the human reference genome (hg19) ($n = 3{,}965$).

For unsupervised hierarchical clustering, we selected the most variably methylated probes across the dataset (s.d. > 0.25). Distance between samples was calculated by using 1 minus the weighted Pearson correlation coefficient as the distance measure. Pairwise Pearson correlation was calculated using the wtd.cors function of the weights package version 0.85. We used the probe standard deviation subtracted by 0.25 as the weight, giving more variable probes greater influence. This matrix was used to perform the *t*-SNE analysis (Rtsne package version 0.11)[57]. The following non-default parameters were used: theta = 0, is_distance = T, pca = F, max_iter = 2,000.

Copy-number variation analysis from 450k methylation array data was performed using the conumee Bioconductor package version 1.0.0. Two sets of 50 control samples displaying a balanced copy-number profile from both male and female donors were used. Scoring of focal amplifications and deletions and chromosomal gains and losses was performed by manual inspection of each

profile. Unsupervised hierarchical clustering of copy-number variation profiles was performed by using 1 minus Pearson correlation coefficient as the distance measure and average linkage for hierarchical clustering.

Differential methylation analysis. Differential methylated probes between groups of human tumor, early PDOX and late PDOX passage were performed as described in Mazor et al.[58]. In short, beta values for individual GpG sites were made more Gaussian using the logit transformation. The transformed beta values were subtracted between patient-matched human tumor, early PDOX, and late PDOX passage and compared using limma (v. 3.6.29)[52]. Differentially methylated CpG were defined as those with a nominal $P > 0.05$ and an average methylation change between groups $>= 0.2$ or $=< -0.2$.

Whole-exome and whole-genome sequencing. The whole-genome libraries, as well as the exome libraries, were prepared according to Agilent SureSelectXT Target Enrichment System for Illumina Paired-End Sequencing Library kit following the manufacturer's instructions. Briefly, genomic DNA was sheared by acoustic fragmentation (Covaris) to an ~300-base-pair (bp) insert size for whole-genome libraries and to a 150–170-bp insert size for exome libraries, followed by size selection. Exome capturing was carried out with Agilent SureSelect Human All Exon V4 or V5 bait library in-solution capture reagents. The quality of the libraries was assessed with the Agilent 2100 Bioanalyzer. Sequencing was done on an Illumina HiSeq2000 instrument with paired-end 100-bp runs or 125-bp runs (v3 and v4) at the DKFZ Genomics and Proteomics Core Facility, Heidelberg, Germany (see Supplementary Table 3).

Whole-genome and -exome sequencing data were processed with a standardized workflow. The alignment and variant calling procedures were adapted from a pipeline developed in the context of the ICGC Pan-Cancer project (https://github.com/ICGC-TCGA-PanCancer). Briefly, reads were aligned to a reference genome using bwa-mem (v. 0.6.2). A merged human and murine reference genome (based on hs37d5 and GRChm38mm10) was used for capturing contaminating reads derived from mouse tissue. Aligned reads were sorted by coordinates and duplicates were marked using biobambam bamSort and bammarkduplicates (v. 0.0.148).

Single-nucleotide variation (snv) calls were based on SAMtools (v. 0.1.19) mpileup and short insertion/deletion (indel) calls on Platypus (v. 0.7.4), followed by specially tailored quality filters taking into account coverage, frequency, and surrounding sequence of variants. Additional filtering was performed by removing mutations in typical artifact genes and positions, which were found mutated at non-hotspot locations in multiple samples, therefore being most likely single-nucleotide polymorphisms or artifacts. Variants were annotated using ANNOVAR (http://annovar.openbioinformatics.org/en/latest/)[59].

Due to lack of availability of the matched germline, we excluded all snvs/indels that fulfilled at least one of the following criteria:

- >0.01% minor allele frequency in 1000g2015aug (in any population) (1,000 Genomes Project)
- >0.01% minor allele frequency in exac03 (in any population) (latest Exome Aggregation Consortium datasets)
- >0.01% minor allele frequency esp6500siv2 (in any population) (latest NSHLBI-ESP project with 6,500 exomes)

Afterwards, we highlighted genes that were reported to be mutated in a reference cohort of primary tumors (only for MB[27] and HGG[26]). Furthermore, we highlighted genes in databases of known cancer genes (http://cancer.sanger.ac.uk/census/)[60], tumor suppressors (http://bioinfo.mc.vanderbilt.edu/TSGene)[61], and oncogenes (http://www.uniprot.org). The entire list of genes can be found in Supplementary Table 4. For comparisons of the mutational landscape of individual human tumors and PDOX, we compared mutation calls of both samples. If mutations were only found in one sample by the variant calling pipeline, we performed an mpileup on that position in the other sample and checked whether this position was covered in this sample. Only mutations that were covered and were negative in the mpileup, were annotated to be lost in the sample. Based on this analysis, the following confidence classes emerged: PASS: mutation called via pipeline; LOW_SCORE: mutation did not pass the quality threshold in this sample, but passed it in the paired tissue; MPILEUP_RESCUE: mutation found in paired tissue and not found in sample via regular variant calling. However, mpileup confirmed the presence of this mutation; MPILEUP_RESCUE_LOW: MPILEUP_RESCUE, except that there were no 10 reads covering the position and/or 3 reads on the mutant base; MANUAL_CURATION: mutation was manually curated (low pipeline score in both tissues); NOT_FOUND: mutation found in paired tissue, but was not detected by either pipeline or mpileup in this tissue; NOT_FOUND_NO_COVERAGE: mutation found in paired tissue, but was not detected by either pipeline or mpileup in this tissue. However, there were no 10 reads covering the position and/or 3 reads on the mutant base (excluded from some analyses); NOT_FOUND_NO_MPILEUP: mutation found in paired tissue, but was not detected by the pipeline in this tissue. However, no mpileup was performed on this position (indel only) (excluded for some analyses).

Copy-number variation plots from low-coverage whole-genome sequencing data were generated by determining the read count within 10-kb windows along the genome in a tumor and a pseudo-control sample without any copy-number alterations, to account for ambiguously covered regions. Coverage is displayed as the $\log_2$ ratio of read counts in tumor versus the control sample, normalized for the total read count in each sample.

RNA sequencing. A tumor DNA library was prepared from poly(A) + RNA using the Illumina TruSeq RNA Kit v2 and sequenced on an Illumina HiSeq2500 (paired-end 100 bp, rapid mode). RNA-seq reads were mapped by STAR algorithm version 2.3.0e[62] using 1,000 genomes as reference for the primary alignment. The index for the alignment was constructed with Gencode version 17 transcript annotations. BAM file conversion and sorting was performed by SAMtools[63] (v. 0.1.17 (r973:277)) and duplicates were marked by Picard version tools (https://github.com/broadinstitute/picard (v. 1.90)). The deFuse (v. 0.6.1) algorithm[64] with default parameters was used for gene fusion predictions.

Animal studies. All animal experiments were conducted in accordance with legal and ethical regulations and approved by the regional council (Regierungspräsidium Karlsruhe, Germany; G-259/14) or IACUC (Seattle). Mice were housed in individually ventilated caging in the Center for Preclinical Research, DKFZ or the Fred Hutchinson Cancer Research Center and monitored daily for the presence of tumor-related symptoms. Sample sizes were chosen to minimize the number of animals required to get significant results.

Preclinical experiments. *Seattle.* Orthotopic xenografts were surgically implanted as described above with tumor cells originating from symptomatic intracranial tumors in donor mice. Adult male and female NSG or athymic nude mice between 8 and 16 weeks of age were used in these experiments. The time between surgical implant of tumors and initiation of treatment was based on the typical latency between surgery and symptomatic tumor for each tumor model. When the first mouse in the cohort became symptomatic with a cranial bulge, the entire cohort was randomized into experimental groups of vehicle or drug treated. Experimental groups were normalized for age, gender, and severity of brain tumor symptoms. Vismodegib-treated mice received 1 mg per mouse of vismodegib (Selleckchem, S1082) by oral gavage, five days on two days off in a vehicle of 0.5% methylcellulose with 0.2% Tween-80 in water. Erlotinib-treated mice received 2 mg per mouse erlotinib (Selleckchem, S7786) by oral gavage in a vehicle of 1% methylcellulose with 0.1% Tween-20 in water, every day for up to 30 days. Panobinostat (Selleckchem, S1030)-treated mice received 10 mg kg^{-1} (NSG host mice, Med-314FH) or 20 mg kg^{-1} (athymic nude host mice, Med-114FH) by intraperitoneal injection, five days on two days off in a vehicle of 48% PEG-200, 2% DMSO, and 2% Tween-80 in water. Palbociclib (LC Labs, P-7788)-treated mice received 100 mg kg^{-1} (NSG host mice, Med-314FH) or 120 mg kg^{-1} (athymic nude host mice, Med-114FH) by oral gavage, five days on two day off in a vehicle of 48% PEG-200, 2% DMSO, and 2% Tween-80 in water. Mice were monitored daily for symptoms of tumor progression until moribund. Tumors were collected after euthanasia and frozen or fixed in 10% formalin. Differences in survival were evaluated using the logrank (Mantel–Cox) test.

Heidelberg. Med-1712FH cells were labeled with luciferase using pGreenFire lentivirus and subsequently after one passage GFP-positive cells were FACS sorted. Cells (100,000) were intracranially injected into the cerebellum of NSG mice. Animals received pre-emptive carprofen analgesia and were anesthetized with isoflurane. Postsurgically, analgesia was continued with carprofen. Twelve weeks after injection, animals were randomized into vehicle (0.5% methyl cellulose/0.5% Tween-80) and erismodegib (MedChem Express, HY-16582) (30 mg kg^{-1}, five days on, two days off) groups according to their luciferase signal and treated for four weeks. For luciferase imaging, animals were injected with 150 mg kg^{-1} Luciferin solution (Promega) and imaged using an IVIS100 or IVIS Lumina luminescence imager with an exposure time of 5 min. Animals were euthanized as soon as they showed tumor-related symptoms or lost more than 20% of their initial weight prior to study entry. After 70 days, we terminated the study. Kaplan–Meier analysis was done using GraphPad Prism, and statistical significance was calculated using a logrank test.

Validation of mutations. Driver/cancer mutations with an allele frequency of at least 20% found in human tumor or early PDOX passages were validated in late PDOX passages by Sanger sequencing. Segments of DNA were amplified via PCR using the HotStarTaq Plus Master Mix Kit (Qiagen, 203643). Primers used for these reactions are listed in Supplementary Table 6. PCR products were purified with the QIAquick PCR Purification Kit (Qiagen, 28106) and sent for Sanger sequencing to GATC Biotech (Konstanz, Germany).

Quantitative reverse transcription PCR for target engagement. For target engagement, tumor-bearing animals were treated with erismodegib 20 mg kg^{-1} (MedChem Express, HY-16582) or vehicle daily by oral gavage for 2 days or vismodegib 1 mg per mouse (Selleckchem, S1082) or vehicle daily by oral gavage for 4 days and then euthanized 4 h after the last dosing. Quantitative reverse transcription PCR (qRT–PCR) was performed from total RNA with the Power SYBR Green RNA-to-CT 1-Step Kit (ThermoFisher Scientific, 4389986) according to the manufacturer's specifications on the 7900HT Fast Real-Time PCR System

(ThermoFisher Scientific). Probes used for qRT–PCR are listed in Supplementary Table 6. Transcript levels were determined by absolute quantification using a standard curve and then normalizing the expression levels to the housekeeping gene *TBP*.

Western blot for target engagement. Mice bearing orthotopic PBT-05FH tumors were treated with 2 mg per mouse erlotinib (Selleckchem, S7786) or vehicle by oral gavage daily for 4 days and euthanized 4 h after the final dose. Mice bearing Med-314FH orthotopic tumors were treated with 10 mg kg^{-1} panobinostat (Selleckchem, S1030) or vehicle by intraperitoneal injection or 100 mg kg^{-1} palbociclib (LC Lab, P-7788) or vehicle by oral gavage daily Monday through Friday. Med-314FH tumors were collected 4 h after the final dose administered to moribund mice. All tumor tissue was collected and stored frozen until further processing. Samples were lysed in Complete M-PER Mammalian Protein Extraction Reagent (ThermoFisher, 78503) with proteases inhibitors (ThermoFisher, A32955) and phosphatase inhibitors (Sigma, P5724 and P0044). From each sample 100 µg for protein extract was run under reducing conditions on a 4–12% Bis-Tris Nu-PAGE gel (ThermoFisher, NP0321) and transferred to a 0.2 µm pore size nitrocellulose membrane (ThermoFisher, LC2000) by semi-dry transfer methods. Immune blotting was performed using standard techniques. Primary antibodies were: EGFR (1:1,000, #4405 S), phospho-EGFR Y845 (1:1,000, #6963 S), phospho-EGFR Y1069 (1:1,000, #2236 S), Acetyl-Histone H3 Lys9 (1:1,000, #9649), RB (1:1,000, #9309), and phospho-RB S780 (1:1,000, #9307) (Cell Signaling Technologies); and b-Actin (1:5,000, #926-4221; Li-Cor). Secondary antibodies used were: IRDye800CW donkey anti-mouse IgG and IRDye680RD goat anti-rabbit IgG (1:15,000, #925-32212 and #925-68071; Li-Cor). Membranes were scanned on a Li-Cor Odyssey CLx Imaging System.

Statistical analysis. Statistical analysis was performed using GraphPad Prism software or the R Statistics environment. Unless otherwise indicated, mean values were always given with a confidence interval of $\alpha = 0.05$. Group comparisons were performed using Student's *t*-test or analysis of variance (analysis of variance), based on whether two or more groups were compared, respectively. Tests were always performed two-sided and adjusted based on whether the variances of the two populations were equal or unequal (*F*-test). Within box plots, the box illustrates the borders of the lower and upper quartile, and the line within the box represents the median. The whiskers highlight the limits of the nominal range inferred from the upper and lower quartiles. To compare engraftment rates and mutation frequencies between populations we used the MedCalc software (https://www.medcalc.org/calc/comparison_of_proportions.php) using the $N-1$ chi-squared test as recommended[65,66]. Weight curves of erlotinib-treated and vehicle-treated animals were compared by performing linear regressions in GraphPad Prism and comparing the slopes. The statistical significance of Kaplan–Meier survival curves was assessed using the logrank (Mantel–Cox) test using GraphPad Prism. *P* values of 0.05 or lower were considered statistically significant for all experiments.

Reporting Summary. Further information on research design is available in the Nature Research Reporting Summary linked to this article.

Data availability

PDOX lines described here, as well as additional lines being developed and characterized, are catalogued online and shared with other researchers at the Brain Tumor Resource Laboratory (http://www.btrl.org). In addition, an online summary of each model and interactive access to the molecular and histopathological data can be found in the R2 PDX Explorer (http://www.r2platform.com/pdxexplorer). Short-read sequencing data are available at the European Genome-phenome Archive (http://www.ebi.ac.uk/ega/), hosted by the European Bioinformatics Institute, under accession EGAS00001002536. Methylation and gene expression data have been deposited in the Gene Expression Omnibus (GEO; http://www.ncbi.nlm.nih.gov/geo) under accessions GSE99994 and GSE99961.

References

50. Lee, J. et al. Tumor stem cells derived from glioblastomas cultured in bFGF and EGF more closely mirror the phenotype and genotype of primary tumors than do serum-cultured cell lines. *Cancer Cell* **9**, 391–403 (2006).
51. Saeed, A. I. et al. TM4: a free, open-source system for microarray data management and analysis. *Biotechniques* **34**, 374–378 (2003).
52. Smyth, G. K. Linear models and empirical bayes methods for assessing differential expression in microarray experiments. *Stat. Appl. Genet. Mol. Biol.* **3**, Article3 (2004).
53. Wilson, C. L. & Miller, C. J. Simpleaffy: a bioconductor package for affymetrix quality control and data analysis. *Bioinformatics* **21**, 3683–3685 (2005).
54. Huang da, W., Sherman, B. T. & Lempicki, R. A. Systematic and integrative analysis of large gene lists using DAVID bioinformatics resources. *Nat. Protoc.* **4**, 44–57 (2009).
55. Huang da, W., Sherman, B. T. & Lempicki, R. A. Bioinformatics enrichment tools: paths toward the comprehensive functional analysis of large gene lists. *Nucleic Acids Res.* **37**, 1–13 (2009).
56. Hovestadt, V. et al. Robust molecular subgrouping and copy-number profiling of medulloblastoma from small amounts of archival tumour material using high-density DNA methylation arrays. *Acta Neuropathol.* **125**, 913–916 (2013).
57. van der Maaten, L. & Hinton, G. Visualizing data using t-SNE. *J. Mach. Learn. Res.* **9**, 2579–2605 (2008).
58. Mazor, T. et al. DNA methylation and somatic mutations converge on the cell cycle and define similar evolutionary histories in brain tumors. *Cancer Cell* **28**, 307–317 (2015).
59. Wang, K., Li, M. & Hakonarson, H. ANNOVAR: functional annotation of genetic variants from high-throughput sequencing data. *Nucleic Acids Res.* **38**, e164 (2010).
60. Futreal, P. A. et al. A census of human cancer genes. *Nat. Rev. Cancer* **4**, 177–183 (2004).
61. Zhao, M., Sun, J. & Zhao, Z. TSGene: a web resource for tumor suppressor genes. *Nucleic Acids Res.* **41**, D970–D976 (2013).
62. Dobin, A. et al. STAR: ultrafast universal RNA-seq aligner. *Bioinformatics* **29**, 15–21 (2013).
63. Li, H. & Durbin, R. Fast and accurate short read alignment with Burrows-Wheeler transform. *Bioinformatics* **25**, 1754–1760 (2009).
64. McPherson, A. et al. deFuse: an algorithm for gene fusion discovery in tumor RNA-Seq data. *PLoS Comput. Biol.* **7**, e1001138 (2011).
65. Campbell, I. Chi-squared and Fisher-Irwin tests of two-by-two tables with small sample recommendations. *Stat. Med.* **26**, 3661–3675 (2007).
66. Richardson, J. T. The analysis of 2×2 contingency tables—yet again. *Stat. Med.* **30**, 890; author reply 891–892. (2011).

nature research

Corresponding author(s): Stefan M. Pfister, Marcel Kool, James M. Olson

Reporting Summary

Nature Research wishes to improve the reproducibility of the work that we publish. This form provides structure for consistency and transparency in reporting. For further information on Nature Research policies, see Authors & Referees and the Editorial Policy Checklist.

Statistical parameters

When statistical analyses are reported, confirm that the following items are present in the relevant location (e.g. figure legend, table legend, main text, or Methods section).

n/a	Confirmed	
☐	☒	The exact sample size (*n*) for each experimental group/condition, given as a discrete number and unit of measurement
☐	☒	An indication of whether measurements were taken from distinct samples or whether the same sample was measured repeatedly
☐	☒	The statistical test(s) used AND whether they are one- or two-sided *Only common tests should be described solely by name; describe more complex techniques in the Methods section.*
☒	☐	A description of all covariates tested
☐	☒	A description of any assumptions or corrections, such as tests of normality and adjustment for multiple comparisons
☐	☒	A full description of the statistics including central tendency (e.g. means) or other basic estimates (e.g. regression coefficient) AND variation (e.g. standard deviation) or associated estimates of uncertainty (e.g. confidence intervals)
☐	☒	For null hypothesis testing, the test statistic (e.g. *F*, *t*, *r*) with confidence intervals, effect sizes, degrees of freedom and *P* value noted *Give P values as exact values whenever suitable.*
☒	☐	For Bayesian analysis, information on the choice of priors and Markov chain Monte Carlo settings
☒	☐	For hierarchical and complex designs, identification of the appropriate level for tests and full reporting of outcomes
☐	☒	Estimates of effect sizes (e.g. Cohen's *d*, Pearson's *r*), indicating how they were calculated
☐	☒	Clearly defined error bars *State explicitly what error bars represent (e.g. SD, SE, CI)*

Our web collection on statistics for biologists may be useful.

Software and code

Policy information about availability of computer code

Data collection	Living Image (PerkinElmer) was used to collect and evaluate bioluminescence signals.
Data analysis	The following software was used for data analysis: R 3.3, GraphPad Prism 5 and 6 Array analysis: R2 (http://R2.amc.nl), simpleaffy (v. 2.46), DAVID 6.7 (https://david-d.ncifcrf.gov/), rtsne (v. 0.11), limma (v. 3.6.29), minfi (v. 1.6.1), conumee (v. 1.0), weights (v 0.85) Whole exome and whole genome sequencing: pipeline developed in the context of the ICGC Pan-Cancer project (https://github.com/ICGC-TCGA-PanCancer), bwa-mem (v. 0.6.2), biobambam (v. 0.0.148), SAMtools (v. 0.1.19), Platypus (v. 0.7.4), ANNOVAR (http://annovar.openbioinformatics.org/en/latest/) RNA sequencing: STAR algorithm version 2.3.0e, SAMtools (v. 0.1.17 (r973:277)), Picard (v. 1.90), defuse (v. 0.6.1)

For manuscripts utilizing custom algorithms or software that are central to the research but not yet described in published literature, software must be made available to editors/reviewers upon request. We strongly encourage code deposition in a community repository (e.g. GitHub). See the Nature Research guidelines for submitting code & software for further information.

Data

Policy information about availability of data

All manuscripts must include a data availability statement. This statement should provide the following information, where applicable:

- Accession codes, unique identifiers, or web links for publicly available datasets
- A list of figures that have associated raw data
- A description of any restrictions on data availability

Short-read sequencing data are available at the European Genome-phenome Archive (http://www.ebi.ac.uk/ega/), hosted by the European Bioinformatics Institute under accession number EGAS00001002536 (developmental page: https://ega-archive.org/studies/EGAS00001002536). Methylation and gene expression data have been deposited in NCBIs Gene Expression Omnibus (GEO, http://www.ncbi.nlm.nih.gov/geo) under accession numbers GSE99994 and GSE99961.

Field-specific reporting

Please select the best fit for your research. If you are not sure, read the appropriate sections before making your selection.

☒ Life sciences ☐ Behavioural & social sciences ☐ Ecological, evolutionary & environmental sciences

For a reference copy of the document with all sections, see nature.com/authors/policies/ReportingSummary-flat.pdf

Life sciences study design

All studies must disclose on these points even when the disclosure is negative.

Sample size	Fig 1-5: Sample size was determined by tumor samples and PDOX models available. Fig 6: Historic use of the included models established an average survival of 8 days after the first mouse becomes symptomatic, with a standard deviation of 4 days. The minimum sample size of 7 allows us to observe significant survival differences greater than 1.5 standard deviation units (6 days) with 80% power in a 2-sided test with 0.05 level of significance. Supplementary Fig. 7: Minimum sample size for target engagement experiments was at least three animals in order to be able to calculate statistical differences. For RT-qPCR (only c,d) analyses three technical replicates were performed per animal (in at least biological triplicates).
Data exclusions	Fig 1-5: NA Fig 6: Mice were excluded from survival studies if they experience and adverse event requiring euthanasia that is unrelated to tumor burden. One mouse was excluded from figure 6A due to error in dosing.
Replication	All attempts at replication were successful.
Randomization	Fig 6: a,b,c,d,g,h: Mice were randomly assigned to treatment groups, balancing for equal males and females in each group. Mice with observable tumor burden (i.e. Head bulge) were evenly and randomly divided between treatment and vehicle groups. Fig 6: e,f: Animals were randomized into treatment groups based on signal intensity.
Blinding	Fig 1-5: NA Fig 6: Animal studies were performed non-blinded due to limited personal. Furthermore, typical side effects (e.g. tooth growth defects observed with SMO inhibitors) identify the treatment groups anyway.

Reporting for specific materials, systems and methods

Materials & experimental systems

n/a	Involved in the study
☐	☒ Unique biological materials
☐	☒ Antibodies
☐	☒ Eukaryotic cell lines
☒	☐ Palaeontology
☐	☒ Animals and other organisms
☐	☒ Human research participants

Methods

n/a	Involved in the study
☒	☐ ChIP-seq
☒	☐ Flow cytometry
☒	☐ MRI-based neuroimaging

Unique biological materials

Policy information about availability of materials

Obtaining unique materials	Established PDOX models are available at www.btrl.org, and all other materials are available from commercial vendors as indicated in the Methods section of the manuscript.

Antibodies

Antibodies used	Brand/Cat#/Lot#/dilution Antibodies used for immunohistochemistry analysis: Primary antibodies: TP53: Proteintech, Rosement, IL/10442-1-AP/1/1:50 PDGFR-a: Santa Cruz Biotechnology Inc., Dallas, TX/Sc-338/A2811/1:100 Olig 2: Immuno-Biological Laboratories/18953/1B-327/1:250 LIN28A: Cell Signaling Technologies, Danvers, MA/3695/2/1:50 GFAP: DAKO, Carpinteria, CA/M0761/00083681/1:400 Ki-67: DAKO, Carpinteria, CA/M7240/00090216/1:100 INI-1: BD Biosciences, San Jose, CA/612110/23247/1:300 EGFR: Invitrogen, Carlsbad, CA/280005/787770 A/1:100 C-MYC: Thermo Scientific, Waltham, MA/MAI-980/OA179819 /1:200 N-MYC: Novus Biologicals, Littleton, CO/23960002/T00308A1 /1:500 Synaptophysin: Abcam, Cambridge, UK/ab32127/GR312544-10/1:300 Beta-Catenin: Abcam, Cambridge, UK/ab16051/GR3185177-1/1:200 GAB-1: Merck Millipore, Burlington, MA/06-579/2942435/1:800 (with a diluent containing Casein [product code #760-219, Roche Ventana]) Secondary ultraView Universal DAB Detection Kit: Ventana Medical Systems, Oro Valley, AZ/760-500/-/- Antibodies used for western blotting analysis: Primary antibodies: EGFR: Cell Signaling Technologies, Danvers, MA/#4405S/4/1:1000 phospho-EGFR Y845: Cell Signaling Technologies, Danvers, MA/#6963S/1/1:1000 phospho-EGFR Y1069: Cell Signaling Technologies, Danvers, MA/#2236S/17/1:1000 Acetyl-Histone H3 Lys9: Cell Signaling Technologies, Danvers, MA/#9649/13/1:1000 RB: Cell Signaling Technologies, Danvers, MA/#9309/11/1:1000 phospho-RB S780: Cell Signaling Technologies, Danvers, MA/#9307/13/1:1000 b-Actin: Li-Cor, Lincoln, NE/#926-42212/C71026-01/1:5000 Secondary antibodies: IRDye800CW donkey anti-mouse IgG: Li-Cor, Lincoln, NE/#925-32212/C70502-03/1:15000 IRDye680RD goat anti-rabbit IgG : Li-Cor, Lincoln, NE/#925-68071/C71214-01/1:15000
Validation	Antibodies used for Immunohistochemistry analysis: All antibodies are first optimized on a set of positive and negative control tissues based on expected staining patterns described in the literature. The full validation workup requires the stain to perform as expected on a set of at least 10 different positive controls and 10 different negative controls. In general full validation includes testing to confirm that antibodies work after freezing (on tissue that was used diagnostically as an intraoperative frozen section), after decalcification, and on autopsy tissues whenever possible. Positive and negative controls are performed every time the antibodies are run. Antibodies used for western blot analysis: All primary antibodies are from Cell Signaling Technologies (Danvers, MA), which performed significant testing of the individual antibodies: “CST scientists test all our products in relevant applications such as western blotting, immunoprecipitation, immunofluorescence, immunohistochemistry, flow cytometry, and chromatin immunoprecipitation. When an antibody is recommend for a particular application, it indicates that the antibody has passed rigorous application-specific testing standards. Additionally, our scientists create specialized (optimized) immunostaining protocols for individual products, saving you time and reagents. We routinely test our antibodies on multiple species including human, monkey, mouse, and rat. The high quality of our products is the most important consideration at CST.” In particular: EGFR (CST #4405S): EGF Receptor (15F8) Rabbit mAb detects endogenous levels of EGF receptor proteins. The antibody does not recognize other proteins of the ErbB family. Product page with citations and validations: https://www.cellsignal.com/products/primary-antibodies/egf-receptor-15f8-rabbit-mab/4405 Data sheet: https://media.cellsignal.com/pdf/4405.pdf

phospho-EGFR Y845 (CST #6963S): Phospho-EGF Receptor (Tyr845) (D63B4) Rabbit mAb recognizes endogenous levels of EGFR protein only when phosphorylated at Tyr845. This antibody may detect other activated ErbB family members.
Product page with citations and validations: https://www.cellsignal.com/products/primary-antibodies/phospho-egf-receptor-tyr845-d63b4-rabbit-mab/6963
Data sheet: https://media.cellsignal.com/pdf/6963.pdf

phospho-EGFR Y1069 (CST #2236S): Phospho-EGF Receptor (Tyr1068) (1H12) Mouse mAb detects endogenous levels of EGF receptor only when phosphorylated at Tyr1068. This antibody does not recognize EGF receptor phosphorylated at other sites, but may cross-react with other activated ErbB family members. Non-specific staining of smooth muscle may be observed in paraffin-embedded tissues.
Product page with citations and validations: https://www.cellsignal.com/products/primary-antibodies/phospho-egf-receptor-tyr1068-1h12-mouse-mab/2236
Data sheet: https://media.cellsignal.com/pdf/2236.pdf

Acetyl-Histone H3 Lys9 (CST #9649): Acetyl-Histone H3 (Lys9) (C5B11) Rabbit mAb detects endogenous levels of histone H3 only when acetylated on Lys9. This antibody does not cross-react with other acetylated histones.
Product page with citations and validations: https://www.cellsignal.com/products/primary-antibodies/acetyl-histone-h3-lys9-c5b11-rabbit-mab/9649
Data sheet: https://media.cellsignal.com/pdf/9649.pdf

RB (CST #9309): Rb (4H1) Mouse mAb detects endogenous levels of total Rb protein. The antibody does not cross-react with the Rb homologues p107 or p130, or with other proteins.
Product page with citations and validations: https://www.cellsignal.de/products/primary-antibodies/rb-4h1-mouse-mab/9309
Data sheet: https://media.cellsignal.com/pdf/9309.pdf

phospho-RB S780 (CST #9307): Phospho-Rb (Ser780) Antibody detects endogenous levels of Rb only when phosphorylated at Ser780. The antibody does not cross-react with Rb phosphorylated at other sites. Product page with citations and validations: https://www.cellsignal.de/products/primary-antibodies/phospho-rb-ser780-antibody/9307
Data sheet: https://media.cellsignal.com/pdf/9307.pdf

Eukaryotic cell lines

Policy information about cell lines

Cell line source(s)	PDOX models and cell lines were generated from patient tissue through the Children's Oncology Group ACNS02B3 brain tumor biology study. Further details about the population characteristics are outlined in the section below (Human research participants: population characteristics).
Authentication	Authentication based on single tandem repeat analysis (STR) and SNPs on Infinium HumanMethylation450 BeadChip. If available these profiles were always compared to the human tumor from which the model system was derived from.
Mycoplasma contamination	All cell lines tested negative for mycoplasma contamination. Results available at www.btrl.org. Overall pathogen testing includes: EBV, Ectromelia, EDIM, HAdV, Hantaan, HCMV, Hepatitis A, Hepatitis B, Hepatitis C, HHV6, HHV 8, HIV1, HIV2, HPV16, HPV18, HSV 1, HSV 2, HTLV 1, HTLV 2, LCMV, LDEV, MHV, MNV, MPV, MVM, Mycoplasma pulmonis, Mycoplasma sp., Polyoma, PVM, REO3, Sendai, Seoul, Sin Nombre, TMEV, VZV
Commonly misidentified lines (See ICLAC register)	NA

Animals and other organisms

Policy information about studies involving animals; ARRIVE guidelines recommended for reporting animal research

Laboratory animals	PDOX development: female Nod-scid IL2Rgammanull (NSG) or athymic nude mice between 8-16 weeks of age Fig 6 a,b,c,d,h; Supplementary Fig. 7 a,b,c,e,f: male and female NSG mice between 8-16 weeks of age Fig 6 e,f; Supplementary Fig. d: female NSG mice between 6-16 weeks of age Fig 6 g; Supplementary Fig. 7 e,f: athymic nude mice between 8-16 weeks of age
Wild animals	The study did not include wild animals.
Field-collected samples	The study did not include field-collected samples.

Human research participants

Policy information about studies involving human research participants

Population characteristics	Patients of the PDOX cohort (n = 30): median age of 6.35 (range 1.8 – 19); gender: n = 17 male, n = 13 female; primary/relapse: n = 21 primary disease, n = 9 relapsed disease (5/9 collected at autopsy), n = 1 NA, entity: n = 2 atypical teratoid/rhabdoid tumor, n = 3 ependymoma, n = 8 high-grade glioma, n = 15 medulloblastoma, n = 2 pineoblastoma.
Recruitment	Model systems were generated through the Children's Oncology Group ACNS02B3 brain tumor biology study.